ACS APPLIED ENERGY MATERIALS

www.acsaem.org Article

Managing Life Span of High-Energy $LiNi_{0.88}Co_{0.11}Al_{0.01}O_2$|C−Si Li-Ion Batteries

Mariyam Susana Dewi Darma,* Jiangong Zhu, Peng Yan, Chenghao Zheng, Martin J. Mühlbauer, Daniel R. Sørensen, Sylvio Indris, Thomas Bergfeldt, Chittaranjan Das, Michael Heere, Liuda Mereacre, Udo Geckle, Anatoliy Senyshyn, Helmut Ehrenberg, and Michael Knapp

Cite This: *ACS Appl. Energy Mater.* 2021, 4, 9982−10002 Read Online

ACCESS | Metrics & More | Article Recommendations | Supporting Information

ABSTRACT: The life span of high-energy cells (3.5 Ah, 18 650, Li-$Ni_{0.88}Co_{0.11}Al_{0.01}O_2$ (NCA)|C/Si, cell type *A*) is investigated as a function of depth of discharges (DoD, between 20 and 100%) and cycling rates (between 1C and C/5). The most relevant degradation mechanism for this cell type is the cycling-induced fracturing of active material. This mechanical degradation of the anode is particularly damaging for the cell life span because it generates chain reactions, i.e., solid electrolyte interphase (SEI) formation. The impedance analysis indicates that electrolyte shortage occurs at the end of life (when the capacity loss exceeds 20%) of all cells, regardless of their cycling protocols. It is revealed that electrochemical activation of the $Li_{0.75}Si$ phase at around 3.0 V causes enormous mechanical stress. Therefore, all of the cells discharged down to 2.65 V show poor lifetime, regardless of their cycling rates and DoDs. The lifetime could be significantly prolonged by cycling the cells above 3.1 V. The scanning electron microscopy (SEM)−energy-dispersive spectrometry (EDX) reveals that some graphite particles are coated by the dense agglomeration of Si particles. The large volume changes of Si might also induce mechanical stress onto the topmost layer of graphite particles underneath the Si coatings, in addition to the mechanical degradation of the Si particle itself.

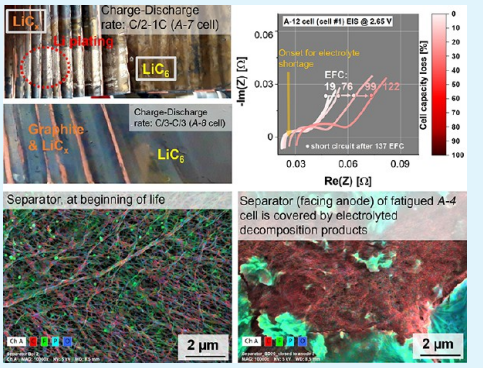

KEYWORDS: *electrolyte shortage, state of health, high-energy cells, Si−C-based anode, electrochemical grinding*

1. INTRODUCTION

The most common arguments for more diverse Li-ion batteries (LIBs) in applications are the ability to provide a balance between high power and high energy densities compared to other types of storage devices, such as supercapacitors and fuel cells. Unlike LIBs, supercapacitors can deliver higher power density, but unfortunately, they cannot provide high energy density.[1] On the other hand, fuel cells can deliver higher energy density but have inferior power densities.

LIB is unquestionably one of today's most relevant enabling technologies. According to market prediction, 60% of the market share of LIBs comes from the automotive sector in 2025.[2] Nevertheless, since around half of the electric vehicle (EV) price corresponds to battery packs, the electric vehicle is still less competitive than the conventional (gasoline-based) one. Therefore, cells with a long life span are crucial to further increasing the EV market share. Battery life span is influenced by several aspects, i.e., cell chemistries (types of active material, electrolyte, and additive), cell design (tab position, cell format, electrode thickness, cell balancing, electrolyte amount, and electrode architecture), and cycling protocols (cycling rate, voltage window, temperature). Furthermore, a longer cell life span is of great importance in achieving sustainable development by reducing the environmental impact of LIBs.[3,4]

The work reported here has several aims: (1) to determine an optimized cycling protocol that can prolong cycle life of the cell, (2) to reveal the most relevant stress factors for cell degradation, (3) to compare the performances of different cell types, and based on those results, (4) the influence of cell design (electrode thickness, electrolyte amount, electrode architecture) on cell performances is discussed.

The underlying degradation mechanisms are studied by both nondestructive and destructive (postmortem) methods. Nondestructive methods such as current−voltage (*I*−*V*) profile analysis, differential voltage analysis (d*V*/d*Q*), differential capacity analysis (d*Q*/d*V*), and electrochemical impedance spectroscopy (EIS) are desirable because they do not require further experiments. Nevertheless, they exhibit limitations, as described in the following.

Received: July 4, 2021
Published: September 15, 2021

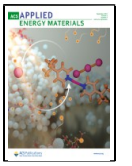

Table 1. Cell Specifications

	type *A*	type *B*	type *C*
cell type	18 650	18 650	18 650
cell mass (g)	48.5	45	46.8
nominal capacity (Ah)	3.5 (1C = 3.5 A)	2.5 (1C = 2.5 A)	3.5 (1C = 3.5 A)
operating voltage, manufacturer's recommendation (V)	2.65−4.2	2.5−4.2	2.5−4.2
cathode			
material	$LiNi_{0.88}Co_{0.11}Al_{0.01}O_2$ (NCA)	42 wt % NCM532 + 58 wt % NCA	$LiNi_{0.83}Mn_{0.07}Co_{0.11}O_2$ (NCM 811)
current collector	Al	Al	Al
dimension [*W* (cm) × *L* (cm)]	6.0 × 60.5	5.7 × 100	6.0 × 62.0
mass density (mg/cm^2)	29	14	30
anode			
material	graphite/Si	graphite/Si	graphite/Si
current collector	Cu	Cu	Cu
dimension [*W* (cm) × *L* (cm)]	6.1 × 64	5.9 × 100	6.0 × 65.7
mass density (mg/cm^2)	16.40	8.10	17.0

The measurable parameters during cycling are voltage and current. It would be great if the degradation mechanisms could be determined solely based on these parameters. However, different degradation processes, such as lithium plating and electrolyte oxidation, might lead to the same *I*−*V* response. Schindler et al. suggested using the increase of current during constant-voltage (CV) charge to indicate lithium plating.[5] This method is suitable for the $LiFePO_4$/graphite cell cycled between 2.0 and 3.6 V. In this low voltage window, electrolyte oxidation is unlikely. However, the current increase during the CV charge could also indicate excessive oxidative parasitic reactions.[6] Meaning that this method suggested by Schindler et al.[5] might not be able to distinguish the lithium plating from electrolyte oxidation for cells operated at higher voltages as, e.g., NCM/$LiNi_{0.88}Co_{0.11}Al_{0.01}O_2$ (NCA)/LMO-based cells.

The d*V*/d*Q* method is often used to quantify the capacity loss of active components of the cells based on the shift of the characteristic peaks of the positive electrode (cathode) and the negative electrode (anode) during cycling/storage.[7−11] Using this method, the capacity losses of electrodes are quantified from the shrinkage of the peak-to-peak distance. The accuracy of the method depends on the precise determination of the peak positions. The characteristic d*V*/d*Q* peaks of materials that undergo solid-state mechanisms such as NCA and NCM are generally broad and weak, causing considerable uncertainty in determining peak positions. Furthermore, the effect of drying out of electrolytes on the contraction of the d*V*/d*Q* curves is neglected in interpreting the curves. It is an open question whether or not this method overestimates the capacity loss of the cathode, anode, and lithium upon drying out of electrolytes.

The differential capacity (d*Q*/d*V*) method provides information on specific-phase degradation, but it cannot be used as a quantitative tool as it is for the d*V*/d*Q* method. Furthermore, the analysis is limited by the fact that the cathode and anode peaks might overlap strongly.

The EIS spectrum contains information on the ohmic resistance of the cells. It is also sensitive to electrochemical polarization resistances at the anode and cathode, such as solid electrolyte interphase (SEI) and charge transfer resistances. Each of these processes rises to a distinct semicircle in the EIS spectra. However, some processes might overlap, and therefore, it is not always possible to deconvolute the EIS spectra. Furthermore, the influence of electrolyte dryout on cell impedance is rarely discussed.

A postmortem analysis provides detailed information on degradation mechanisms, complementing the nondestructive methods. By understanding the underlying degradation mechanism of a cell, one can then suggest how to improve the cell design, which is also part of the discussion in this report.

In our study, both nondestructive and destructive methods were performed to reveal the degradation mechanisms of commercial cells with a nominal capacity of 3.5 Ah, labeled as type *A*. This cell type employs $LiNi_{0.88}Co_{0.11}Al_{0.01}O_2$ (NCA) as a cathode and a composite C/Si as an anode. Thirty cylindrical cells of type *A* were cycled at 25 °C under different voltage windows and cycling rates (12 cycling protocols in total). The cell specification, cycling protocols, and experimental methods are described in Section 2. The cycling test results of the type *A* cells are categorized based on the nondestructive method (Section 3.1) and postmortem analysis (Section 3.2). Complementary experiments including electrochemical cycling, X-ray diffraction (XRD), magic angle spinning nuclear magnetic resonance (MAS NMR), and inductively coupled plasma−optical emission spectrometry (ICP−OES) were carried out to investigate capacity losses of cell components, transition-metal dissolution, and Li-plating. The mechanical degradation of either electrode is quantified from the increase of Brunauer−Emmett−Teller (BET) surface area estimation after cycling. The phase-specific mechanical degradation of the C/Si anode is qualitatively investigated by scanning electron microscopy−energy-dispersive X-ray spectroscopy (SEM−EDX). The effect of cell designs (electrode thickness, particle morphology) on cycling performances is investigated by comparing type *A* cells with type *B* and *C* cells. All cell types employ the same format of 18650 cylindrical cells. Types *A*, *B*, and *C* consist of NCA, NCA&NCM, and NCM cell chemistry, respectively, and exhibit slightly different cell designs. The performance comparison of these three cells is given in Section 4.

2. EXPERIMENTAL SECTION

2.1. Cell Specifications. Table 1 presents detailed specifications of cells of types *A*, *B*, and *C*. Note that 1C is defined according to its nominal capacity, i.e., 3.5 A for cell types *A* and *C* and 2.5 A for cell type *B*. The electrode compositions for the cell types *A* and *C* given in

https://doi.org/10.1021/acsaem.1c01946
ACS Appl. Energy Mater. 2021, 4, 9982−10002

Table 2. Cycling Protocols

Cycling protocol (number of cells)	Charge – Discharge Rate	Voltage window [V]	SoC range at BoL [%]	Remarks
A-1 **(3)**	1st – 222nd EFC: C/2- 1C	2.65 V – 4.2 V	0 % -100 %	*Post-mortem* analyses were performed for cell#1 after 252 EFCs and cell #3 after 137 EFCs.
	Cell#1: 223rd – 231st EFC: C/2- 1C 232nd – 242nd EFC: C/10 – C/10 243rd – 252nd EFC: C/20- C/20	2.65 V – 4.2 V	0 % -100 %	
	Cell#2: 223rd – 227th EFC: C/5 – C/5 228th – 235th EFC: C/20- C/20	2.65 V – 4.2 V	0 % -100 %	
A-2 **(3)**	C/3 – C/3	2.65 V – 4.2 V	0 % -100 %	All cells short-circuited after 162-190 EFCs.
A-3 **(3)**	C/2 – 1C	Constant Q_{charge} 1.3 Ah from 2.65 V. Upper voltage limit: 4.2 V (0 % SoC – 37 % SoC)		
A-4 **(3)**	C/5 – C/5			All cells short-circuited after 100 – 130 EFCs
A-5 **(3)**	C/2 – 1C	Constant $Q_{discharge}$ 1.3 Ah from 4.2 V. Lower voltage limit: 2.65V (63 % SoC – 100 % SoC)		
A-6 **(3)**	C/5 – C/5			
A-7 **(2)**	1st – 293rd EFC: C/2 – 1C	3.1 V – 4.1 V	10 % - 83 %	Cell #1 short-circuited after 520 EFCs
	After 294th EFC: C/3 – C/3	3.1 V – 4.1 V	10 % - 83 %	
A-8 **(3)**	C/3 – C/3	3.1 V – 4.1 V	10 % - 83 %	
A-9 **(2)**	Cell #1: 1st – 128th EFC: C/2 – 1C 128th – 192nd EFC: C/5 – C/5	 3.1 V – 4.2 V 3.1 V – 4.1 V	 10 % - 100 % 10 % - 83 %	
	Cell #2: 1st – 159th EFC: C/2 – 1C 160th – 201st EFC: C/5 – C/5	 3.1 V – 4.2 V 3.1 V – 4.1 V	 10 % - 100 % 10 % - 83 %	
A-10 **(2)**	C/3 – C/3	3.1 V – 4.2 V	10 % - 100 %	
A-11 **(2)**	1st – 332nd EFC: C/2 – 1C	2.9 V – 4.1 V	8 % - 83 %	
	After 333rd EFC: C/3 – C/3	3.1 V – 4.1 V	10 % - 83 %	
A-12 **(1)**	C/5 – C/5	constant Q_{charge} 700 mAh from 2.65 V. Upper voltage limit: 4.2 V (0 % SoC – 20 % SoC)		Short-circuited after 137 EFCs
B-1 **(1)** [7]	1C – 1C	2.5 V – 4.2 V	0 % - 100 %	
C-1 **(2)**	C/2-1C	2.5 V – 4.2 V	0 % - 100 %	

Table 1 are taken from ref 12. The electrode composition of cell type *B* is taken from ref 7.

2.2. Cycling Protocols. Instead of cycle number (n), the cycling performances of the cells are presented as a function of the equivalent full cycle (EFC) to ensure a fair comparison between cells cycled with different charge capacities. The EFC is defined as

$$\mathrm{EFC} = \frac{\sum_1^n (Q_{\mathrm{charge}} + Q_{\mathrm{discharge}})}{(Q_{\mathrm{charge}} + Q_{\mathrm{discharge}})_{\mathrm{BoL}}}$$

The cycling protocols for the cells of type *A* are listed in Table 2. Before the cycling test, the cells were cycled between 2.65 and 4.2 V at a charge/discharge rate of C/10 for five cycles to ensure a uniform formation step. Afterward, the cell capacity at the beginning of life (BoL) was determined at a rate of C/25.

The cells were cycled either within a constant-voltage window or for a constant capacity (1.3 or 0.7 Ah). Three different cycling rates were used, abbreviated as high rate (HR, charge−discharge rate of C/2−1C), low rate 1 (LR1, charge−discharge rate of C/3−C/3), and low rate 2 (LR2, charge−discharge rate of C/5−C/5). All tests were conducted using a multichannel potentiostat (BCS BioLogic Science Instruments) at 25 °C.

The cells are labeled as *A-X* (cell #*Y*), where *X* reflects the cycling protocol from 1 to 12 and *Y* refers to the number of the cells (1, 2, or 3) that were cycled under identical *A-X* protocol. At least two cells were cycled for each protocol, except for the *A-12* protocol.

The cells that were cycled within a constant-voltage window (*A-1*, *A-2*, *A-7* to *A-11*), charged with a constant current−constant-voltage (CC−CV) mode and discharged with a constant current (CC) mode. The cutoff current for the constant-voltage (CV) charge was C/20 and the resting period after charge and discharge was 30 min. The *A-1*, *A-7*, *A-9*, and *A-11* cells were initially cycled at a high rate (HR1) until their capacities decreased significantly. Afterward, these cells were further cycled with lower rates of C/3, C/5, C/10, or C/20 (see Table 2) to investigate whether or not these cells could still deliver high capacity at lower rates. The voltage profiles of all of the cells are presented in the Supporting Information (Figure S1 for the cells cycled in a constant-voltage window, and Figure S2 for the cells cycled for a constant capacity).

The cells of types *B* and *C* serve as comparisons to the *A-1* cells. The *C-1* cells were charged with CC−CV mode (cutoff current C/20 during CV charge), while the *B-1* cell was charged without the CV charge step. Note that the cycling performance of the *B-1* cell has been previously reported in ref 7 (labeled as CY25-CC-700 cell in this report).

The remaining cell capacity was monitored every 50 cycles at a rate of C/25. The capacity loss is then calculated based on the decrease of capacity at the nth cycle, relative to the cell capacity at BoL. Galvanostatic electrochemical impedance spectroscopy (GEIS) was also carried out every 50 cycles in the frequency range of 10 kHz to 10 mHz, and with a sinusoidal current of 1 A. Initially, the GEIS spectra were recorded at 2.65 V; however, it is challenging to interpret the EIS spectra at 2.65 V of the fatigued cells. It seems that the Warburg diffusion overlaps strongly with other processes in the low-frequency region. Therefore, we amended the protocol to add EIS measurements at 3.9 V. The impedance data were evaluated using the commercial RelaxIS software.

2.3. Postmortem Analysis. For postmortem analysis, selected cells at different fatigued states were opened in the discharged state

https://doi.org/10.1021/acsaem.1c01946
ACS Appl. Energy Mater. 2021, 4, 9982−10002

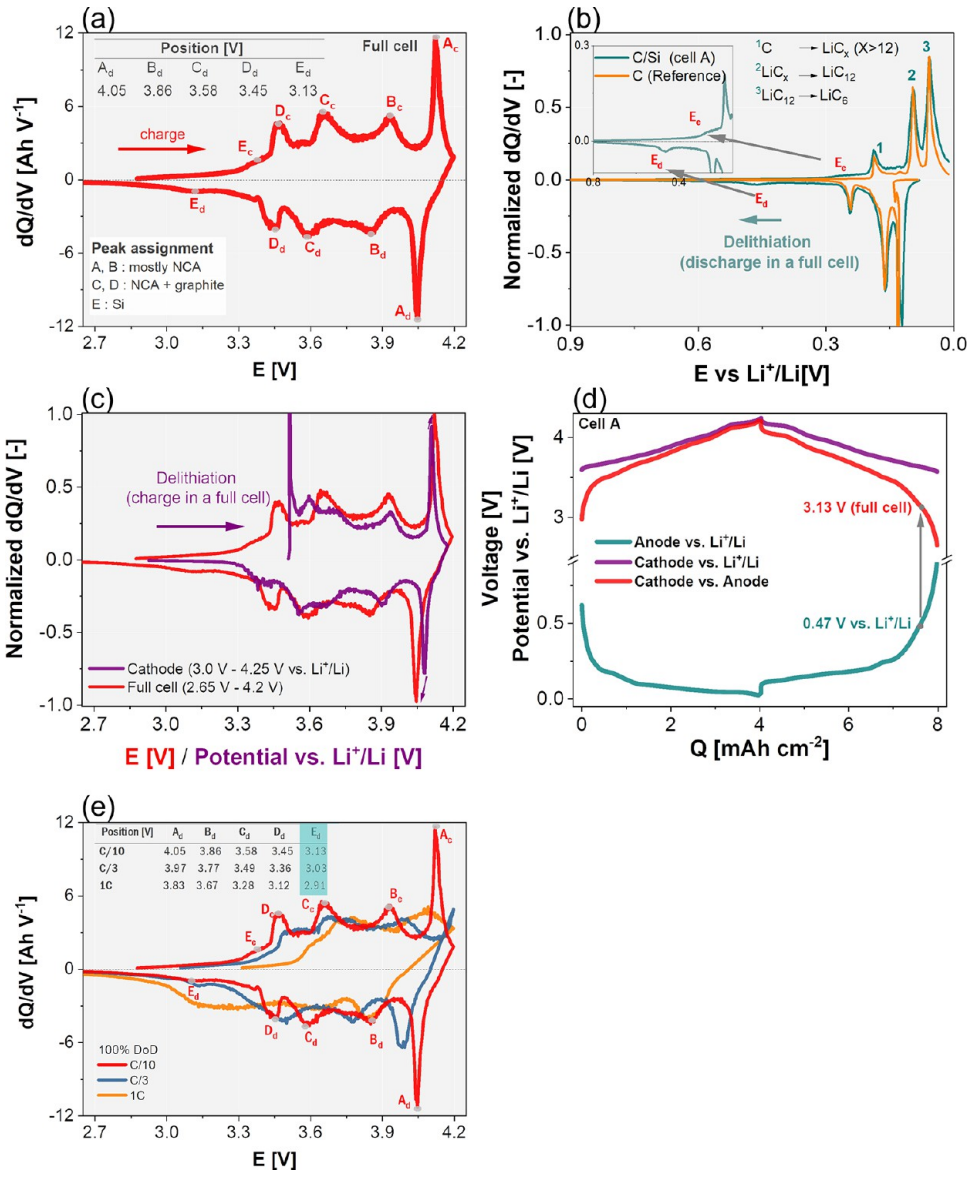

Figure 1. dQ/d*V* plots at a rate of C/10: (a) for the full cell of type *A* at BoL and its corresponding as opened (b) anode and (c) cathode cycled versus lithium in the half-cell geometry. The dQ/d*V* values of the anode and cathode are normalized to the maximum value. (d) Three-electrode measurement result of the cathode vs anode taken from cell type *A* (at BoL) using lithium metal as the reference electrode. (e) Rate-dependent dQ/d*V* curves of cell type *A*.

(2.65 V) in a glovebox (MBraun) filled with Ar, where the H_2O and O_2 concentrations were held below 0.1 ppm.

2.3.1. Electrochemical Measurements. One side of the double-coated electrodes was removed for further electrochemical tests using dimethyl carbonate (DMC). An electrode with a diameter of 12 mm was then punched out. Electrochemical measurements were carried out in the three-electrode and half-cell configurations at different rates using a multichannel potentiostat (VMP, BioLogic). The current was calculated based on the nominal capacity of the cell, divided by the total area of the cathode (1C = 4.8 mA/cm^2 for cell types *A* and *C*, and 1C = 2.2 mA/cm^2 for cell type *B*). All electrochemical measurements utilized 1 M $LiPF_6$ in ethylene carbonate/dimethyl carbonate (EC/DMC, 1:1 v/v, LP30 from Merck) as the electrolyte.

Three-electrode Swagelok cells were used for three-electrode measurements where the cathode (taken from the BoL and *A-1* cells) was cycled against the anode (taken from the BoL and *A-1* cells) with lithium metal as the reference electrode. The cells were charged in a CC−CV mode at a rate of C/3 or C/10, with a cutoff current of C/20. The cells were discharged in a CC mode. For this measurement, glass-fiber-based Whatman separators were used. Half-cell measurements consisting of an electrode sheet, a Celgard separator, and lithium metal were carried out in a CR 2025 coin cell.

2.3.2. X-ray Diffraction. Structural analysis of the electrodes was performed by XRD. Three different sample preparations were used, i.e., as opened, ex situ, and in operando XRD samples. The as opened samples were taken directly after cell opening and then sealed between two Kapton tapes to ensure airtightness during the measurements. Before performing ex situ XRD experiments, the anodes of types *A* and *B* (at BoL) were prelithiated at a rate of C/10. A dedicated coin cell with a 75 μm Kapton foil window was used as a sample container to avoid air contact.[13] As opened and ex situ XRD experiments were performed using Mo Kα_1 radiation (λ = 0.70932 Å) in a transmission geometry at a STOE STADI/P diffractometer (Ge 111 monochromator, Mythen 1D silicon strip detector).

In operando XRD measurements were performed using a dedicated in operando setup.[13] The diffractometer has a Ag X-ray tube (λ = 0.55941 Å) with a focusing Ge 111 monochromator and two Mythen 1D silicon strip detectors. The cathode was cycled against lithium metal at a rate of C/10 between 3.0 and 4.25 V using a galvanostatic

https://doi.org/10.1021/acsaem.1c01946
ACS Appl. Energy Mater. 2021, 4, 9982−10002

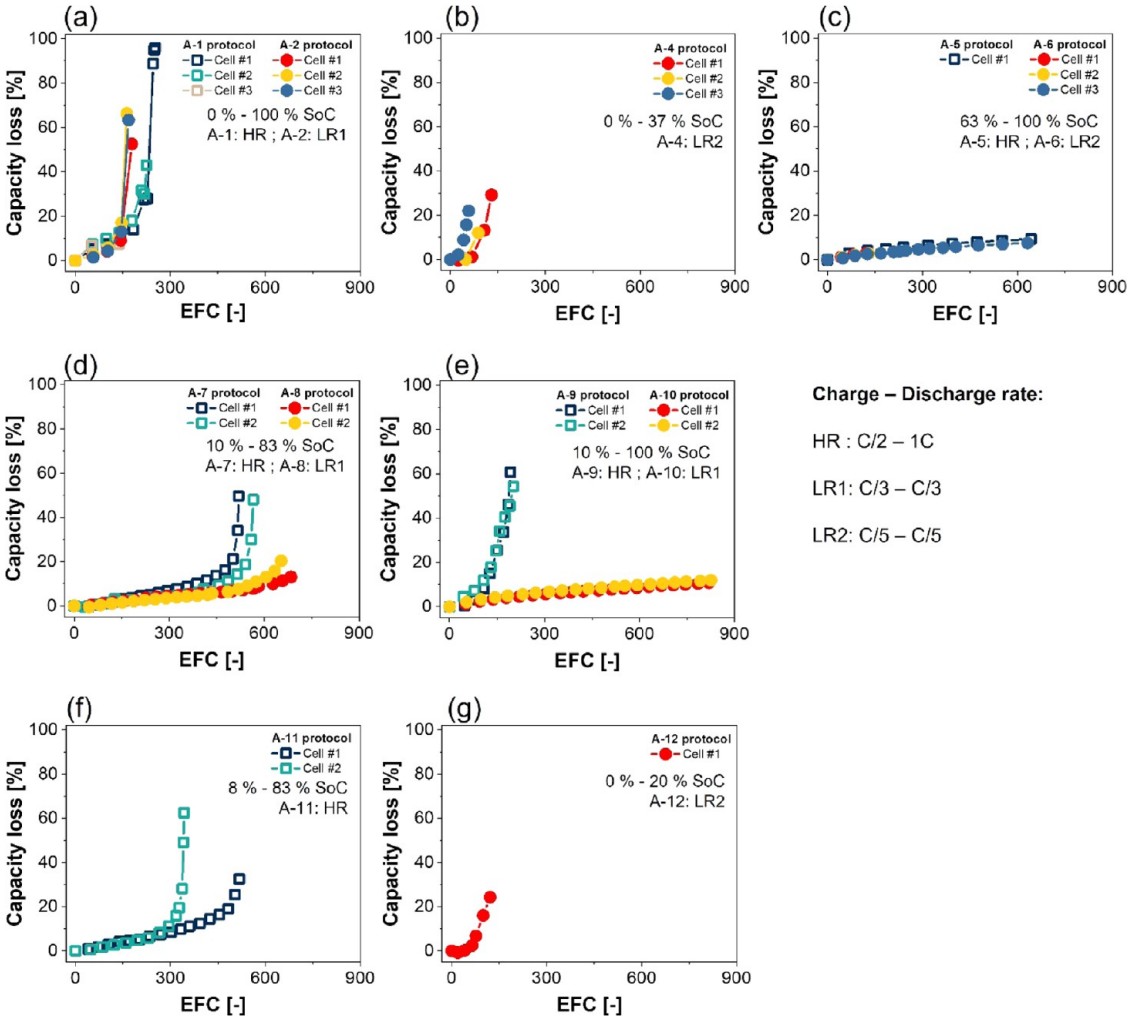

Figure 2. (a–g) Capacity losses of type *A* cells as a function of EFC for different cycling conditions.

system μAUTOLAB-FRA2, TYPE III controlled by NOVA. The acquisition time was 20 min per pattern with stationary detectors.

Structural refinements were carried out by the Rietveld method using FullProf software.[14] The instrumental resolution function was determined from the half-width of the LaB_6 standard (NIST 660b).

2.3.3. ^{7}Li Magic Angle Spinning Nuclear Magnetic Resonance. ^{7}Li MAS NMR experiments were performed on a Bruker Avance 200 MHz system at a magnetic field of B_0 = 4.7 T, which corresponds to a ^{7}Li Larmor frequency of 77.8 MHz. An aqueous solution of 1 M LiCl was used as a reference for the chemical shift of ^{7}Li at 0 ppm. Spectra were acquired in 1.3 mm zirconia rotors at a spinning speed of 40 kHz and with a rotor-synchronized Hahn-echo pulse sequence at a $\pi/2$ pulse length of 1 μs and a recycle delay of 1 s.

2.3.4. Brunauer–Emmett–Teller Method. The surface area of the electrodes was determined through N_2-adsorption with evaluation by the BET method (Gemini VIII 2390, Micromeritics). The samples for BET measurements were collected from around 20 to 25% of the total electrode area of the as opened cells to ensure representative results.

2.3.5. Scanning Electron Microscopy–Energy-Dispersive X-ray spectroscopy. The electrode morphology was investigated by thermal field emission (FE) SEM, using a ZEISS Merlin ⟨5 kV, in-lens detector). The elemental distribution on the sample surface was studied by EDX using a Bruker Quantax 400 system attached to the SEM.

2.3.6. Inductively Coupled Plasma–Optical Emission Spectroscopy. The cathode and anode compositions were determined by ICP–OES (iCAP 7600 from Thermo Fisher Scientific). For this experiment, the samples were dissolved in hydrochloric acid and nitric acid at 353 K in a graphite oven (Analab). The elemental analysis was conducted using four different calibration solutions and two internal standards (sodium and scandium). The oxygen content was determined by carrier gas hot extraction (CGHE).

2.3.7. EIS on Cathode and Anode. Potentiostatic electrochemical impedance spectroscopy (PEIS) of each electrode was also carried out in a half-cell configuration in the frequency range of 1 MHz to 1 mHz and with a sinusoidal potential of 10 mV.

3. RESULTS: DEGRADATION OF TYPE *A* CELLS

Except otherwise mentioned, this section presents the cycling performances of type *A* cells.

3.1. Cycling Tests. In this section, the influence of the state of charge (SoC), depth of discharge (DoD), and cycling rate on cycling stability are discussed. The underlying degradation mechanisms are investigated based on the d*Q*/d*V* plot and EIS evolution during cycling.

3.1.1. dQ/dV Analysis. The d*Q*/d*V* curves of the type *A* cell at BoL are plotted against voltage in Figure 1a. Four characteristic peaks (A–D) and a shoulder E are observed. One cell of type *A* at BoL was opened to identify these peaks and the shoulder. The as opened anode and cathode at BoL were then cycled against lithium in a half-cell geometry at a rate of C/10. Their corresponding d*Q*/d*V* plots are presented in Figure 1b,c, respectively. The anode potential (*x*-axis in Figure 1b) is given in a reversed order, in the same direction

https://doi.org/10.1021/acsaem.1c01946
ACS Appl. Energy Mater. 2021, 4, 9982–10002

during charge in full cells. With the help of potential profiles measured in three-electrode geometry (Figure 1d), the positions of the electrode peaks found in this half-cell setup are then correlated to the voltage in the full cell.

Figure 1b shows the dQ/dV plot of the C/Si-based anode taken from the cell of type *A*, showing electrochemical activities of the graphite and Si phases. The dQ/dV plot of the graphite-based anode is overlaid in this figure as a reference. Three characteristic peaks (labeled as 1, 2, and 3) are associated with the transformation of graphite into LiC_x ($x > 12$), LiC_{12}, and LiC_6 phases during charge and vice versa during discharge. A shoulder at ∼0.25 V vs Li^+/Li during lithiation (at 0.47 V vs Li^+/Li during delithiation) is associated with the $Li_{0.75}Si$ phase.[15] Apart from this peak, three other Li_ySi peaks ($0.75 < y < 3.75$) are expected between 0.25 and 0.02 V.[15,16] However, these peaks overlap with the lithiated graphite peaks. Since the anode has only 2 wt % of Si, it is difficult to identify Li_ySi peaks ($0.75 < y < 3.75$) in Figure 1b.

According to the anode potential profile in the three-electrode measurement presented in Figure 1d, the lithiated silicon peak (E_d) at 0.47 V vs Li^+/Li corresponds to the peak E_d at 3.13 V in the full cell (see Figure 1a,d).

The dQ/dV plot of the cathode (purple curve) is shown in Figure 1c, superimposed with that of the full cell (red curve). It is shown here that the dQ/dV curve of the cathode is similar to that of the full cell. The peak B_c of the full cell in Figure 1a associates mainly with the cathode peaks. The strong overlapping between cathode and anode peaks influences the positions of peaks A, C, and D in the full cell.

As seen in Figure 1e, the dQ/dV curve strongly depends on the cycling rates. At a rate of C/10, all characteristic peaks are easily identified. All peaks shift to lower voltages during discharge at higher rates (and vice versa during charge). An example is peak E_d, found at 3.13 V at C/10, which shifts to ∼3.07 V at C/3. At 1C, some peaks overlap, making it more challenging to distinguish electrochemical activities of different phases. At this rate, a broad plateau-like feature is observed in the region of 3.45 and 3.1 V, rising from a strong overlapping between peak D_d and C_d. It seems that the tail of this plateau at around 2.91 V corresponds to the peak E_d.

3.1.2. Influence of Cycling Parameters on the Capacity Decay. The evolution of capacity losses is presented as a function of EFC in Figure 2 for different cycling conditions. The capacity losses of the cells cycled under the same voltage ranges but at different cycling rates (e.g., *A-1* and *A-2* cells or *A-7* and *A-8* cells) are presented in the same plot. In this way, the influence of the cycling rate on capacity decay can be directly spotted.

It is evident that capacity loss does not increase linearly with the EFC number. The cell capacity decreases gradually at the beginning of the cycling test. However, faster capacity decays occur after the cells reach a certain degree of fatigue. The onset of this accelerated degradation depends strongly on the cycling protocols. For the cells discharged down to 2.65 V, i.e., the *A-4* cells (0−37% SoC, LR2), the *A-12* cell (0−20% SoC, LR2), *A-1* cells (100% DoD, HR), and *A-2* cells (100% DoD, LR1), the accelerated degradation is detected already before 150 EFCs, even when the cells are cycled at low rates of C/3 or C/5. These results are unexpected since type *A* cells are categorized as high-energy cells whose primary purpose is to deliver high capacity at a low rate.

A longer life span is found for the *A-5* (HR) and *A-6* (LR2) cells cycled between 63 and 100% SoC. The accelerated degradation is not observed even though these cells have been cycled for 600 EFCs. Within this narrow DoD, cycling rates have a minor effect on the cell life span. A slow capacity decay is also found for the *A-10* (LR1) cells, cycled in a broad DoD between 10 and 100% SoC. The average capacity loss of the two cells cycled under the *A-10* protocol after 820 EFCs is less than 12%. In fact, the optimum cycling conditions for type *A* are found to be in the *A-10* protocol.

At first glance, some results seem to be counterintuitive. It is generally accepted that broadening the DoD would result in faster cell degradation.[17] However, it is not always the case for type *A* cells. The cell life span of the *A-12* cell (Figure 2g) that was cycled at 20% DoD is much shorter than the *A-10* cells (Figure 2e) that were cycled at 90% DoD.

Surprisingly, the influence of cycling rate on life span is nearly negligible for the cells discharged down to 2.65 V (*A-1* vs *A-2* cells or *A-3* vs *A-4* cells). The influence of cycling rates on cycling stability is only observed for the cells cycled above 3.1 V and at broader DoDs, e.g., for *A-7* vs *A-8* cells and *A-9* vs *A-10* cells. For these cells, increasing cycling rates shorten their life span.

Even though studies on degradation mechanisms related to LIBs are abundant (see Table 3), investigating the degradation mechanisms of commercial cells is still challenging. Two or more degradation mechanisms listed in Table 3 might simultaneously occur during cell operation. For lifetime studies, it is imperative to identify and estimate the degradation rate of the most relevant degradation mechanism occurring at specific cycling parameters, which is unfortunately rarely available in the literature. It is still unclear, for example, which one is more detrimental for the cell lifetime: cathode−electrolyte interface (CEI) formation, transition-metal dissolution, or mechanical degradation.

Table 3. Reported Degradation Mechanisms

proposed degradation mechanisms		references
cathode	CEI formation	occurred at a high voltage; 18−20
	cathode instability at a high voltage (defined by the maximum c/a ratio, where c and a are lattice parameters)	17, 21
	mechanical degradation	22−26
	transition-metal dissolution	27−29
	formation of an inactive phase	30
anode	SEI formation	18, 19, 31−36
	reduction of additives such as fluoroethylene carbonate (FEC)	∼0.9 V vs Li^+/Li; 37−39
	mechanical stress due to (de) lithiation of graphite or Si	23, 25, 40, 41
	Li plating	42−44

As seen in Figure 2, the degradation rate of the cell is not constant during its life. However, to provide a more quantitative measure in comparing the cell performance, the average degradation rates of type *A* cells is estimated by dividing the capacity loss by the number of EFCs until the cell reached the end of life (EoL, i.e., when the capacity loss exceeds 20%), except for the A-5, A-6, and A-10 cells. These cells have not reached the EoL yet; therefore, their average degradation rates are calculated based on the capacity losses at the end of cycling, around 10−11%. However, this slightly different estimation procedure would not change the fact that

https://doi.org/10.1021/acsaem.1c01946
ACS Appl. Energy Mater. 2021, 4, 9982−10002

degradation rates are the lowest for the A-5, A-6, and A-10 cells.

The estimated average degradation rates of type *A* cells are presented in Figure 3, with the color scale is associated with the estimated degradation rate. The average degradation rates of type *A* cells spread between 0.01%/EFC for the *A-6* cells (the lowest) and 0.18%/EFC for the *A-12* cell (the highest rate). The references cited in Table 3 help determine the possible degradation mechanisms for these two cells, summarized in the following.

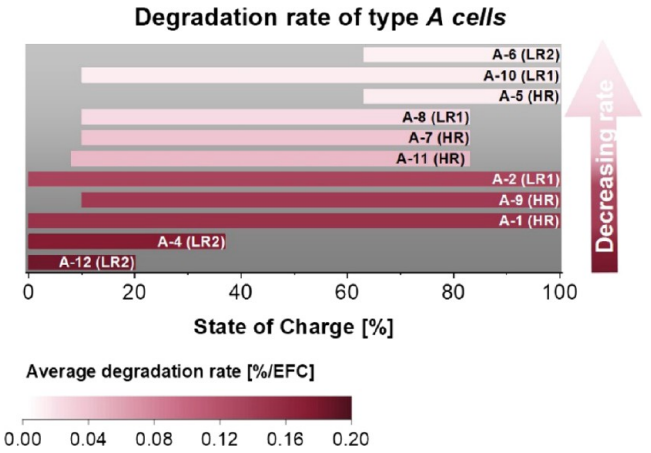

Figure 3. Degradation rates of type *A* cells cycled at various SoC and DoD. The procedure to estimate the average degradation rate is described in the text.

In the low-voltage region (the case for the *A-12* cell), the cell degradation might be associated with several mechanisms: mechanical degradation due to the transformation of Si to $Li_{0.75}Si$ and graphite to LiC_x ($x \geq 12$) at the anode side, mechanical degradation due to the lattice changes of NCA and SEI formation. However, it is still challenging to determine which degradation reaction has the highest rate.

In the higher-voltage region (the case for the *A-6* cells), the cell degradation might be associated with the formation of CEI layer, instability of the layered oxides as positive electrode materials at high potential,[21] mechanical degradation due to the lattice expansion/contraction of NCA at the cathode side, and mechanical degradation at the anode side due to the transformation of LiC_{12} to LiC_6 phase and formation of Li_ySi ($0.75 < y < 3.75$).

Since the degradation rates for most of the cells cycled above 3.1 V are low, i.e., for the *A-5* to *A-8* and *A-10* cells, it is concluded that the most degrading reactions occur below 3.1 V. This is in agreement with the fact that the degradation rate of the *A-12* cell is one order of magnitude higher than the *A-6* cell.

Besides accelerated degradation, short circuits also occur for highly degraded cells (capacity loss >40%). Before the short circuit, the dI/dt during the constant-voltage charge at 4.2 V increased rapidly (see the $I-V$ profiles in Figure S3), in contrast to the decrease of dI/dt in healthy cells. In fact, this unusual current profile was detected few cycles before the cell finally died. Thus, $dI/dt > 0$ during CV charge could be used as one criterion for a poor state of health (SoH).

3.1.3. Evolution of the Cell Impedance during Cycling. Figure 4 presents the evolution of EIS at 3.9 V for selected cells, representing those that degraded at fast (a, b), moderate (c, d), and slow (e, f) rates. The EIS spectra for all other cells are given in Figure S4. The color scale correlates the measured impedance to the capacity loss. The EFC number is indicated above the corresponding spectrum.

It is instantly evident from Figure 4 that when the capacity loss increases gradually, its corresponding impedance grows slowly, too. On the other hand, the sudden jump of the EIS coincides with the rapid increase of capacity loss, and it is observed only for the cells with high and moderate degradation rates (Figure 4a–d).

An EIS spectrum provides a lot of information on the electrochemical processes occurring in a distinct frequency region. In the high-frequency region, the EIS spectrum correlates to the inductance (I), ohmic resistance (R_0), and transport resistances through SEI and CEI (R_{SEI}, R_{CEI}), while the spectrum in the medium-frequency region correlates to the charge transfer resistance (R_{CT}). A straight line with a phase angle of 45° in the low-frequency region reflects the Warburg diffusion (W).

The example for the equivalent circuit model (ECM) to fit the spectra is shown in the inset of Figure 5a. For most cases, the R_{SEI}, R_{CEI}, $R_{CT\text{-cathode}}$, and $R_{CT\text{-anode}}$ values of type *A* cells overlapped strongly, rising to only one semicircle in the high- to medium-frequency region. Therefore, only one RQ element (CPE_1, R_1) is used to fit this semicircle, with R_1 representing the total resistance of all electrochemical processes.

The Warburg diffusion overlaps with another process in the low-frequency region, modeled as the second RQ element (CPE_2, R_2). The use of R_2 slightly improves the fitting results; see, e.g., the *A-7* cell in Figure 5a. The exact nature of the R_2 is unclear, but at such low frequencies, the EIS response might be influenced by nonelectrochemical processes, such as ion transport in electrode pores and ion adsorption in the porous network.[1,45] The magnitude of R_2 is one order of magnitude lower than that of R_1, but it has a larger CPE. The CPE is used instead of pure capacitance because it can well describe the porous electrode.[46] Figure 5a shows that the measured impedance at $-\mathrm{Im}(Z) = 0$ is labeled as ohmic resistance R_0. The fitted R_0 deviates slightly from the value at $-\mathrm{Im}(Z) = 0$ because it overlaps with the cell inductance (I). The accuracies for fitted R_2 and W values are low because the two parameters are highly correlated. Therefore, they are not interpreted further in this manuscript.

The fitted R_0, R_1, and W at 3.9 V are given in Figure 5b–d. The impedance evolution differs significantly for the cells cycled at lower-voltage (2.65 to ~3.7 V, A-12 cell) and higher-voltage windows (~3.75–4.2 V, *A-6* cell). As seen in Figure 5b, the impedance increase of the *A-6* cell is dominated by the large increase of R_1, compared to the small increase of its corresponding R_0. On the other hand, both the R_0 and R_1 of the A-12 cell increase gradually until the cell loses roughly 7% of its initial capacity. Afterward, the R_1 of the *A-12* cell increases faster than its R_0.

The charge transfer resistance grows faster than the transport resistance through the SEI or CEI.[7] Therefore, it is speculated that the impedance increase of the *A-6* cell correlates mainly with the rise in R_{CT}. On the other hand, the electrolyte decomposition leads to a slight rise in ohmic (R_0) and faradaic (R_1) resistances, as evident from the *A-12* cell at the beginning of cycling.

The EIS evolution for the *A-6* and *A-12* cells can be used as fingerprints to understand the degradation mechanisms of all other cells. The impedance evolution of the *A-8* and *A-10* cells

https://doi.org/10.1021/acsaem.1c01946
ACS Appl. Energy Mater. 2021, 4, 9982–10002

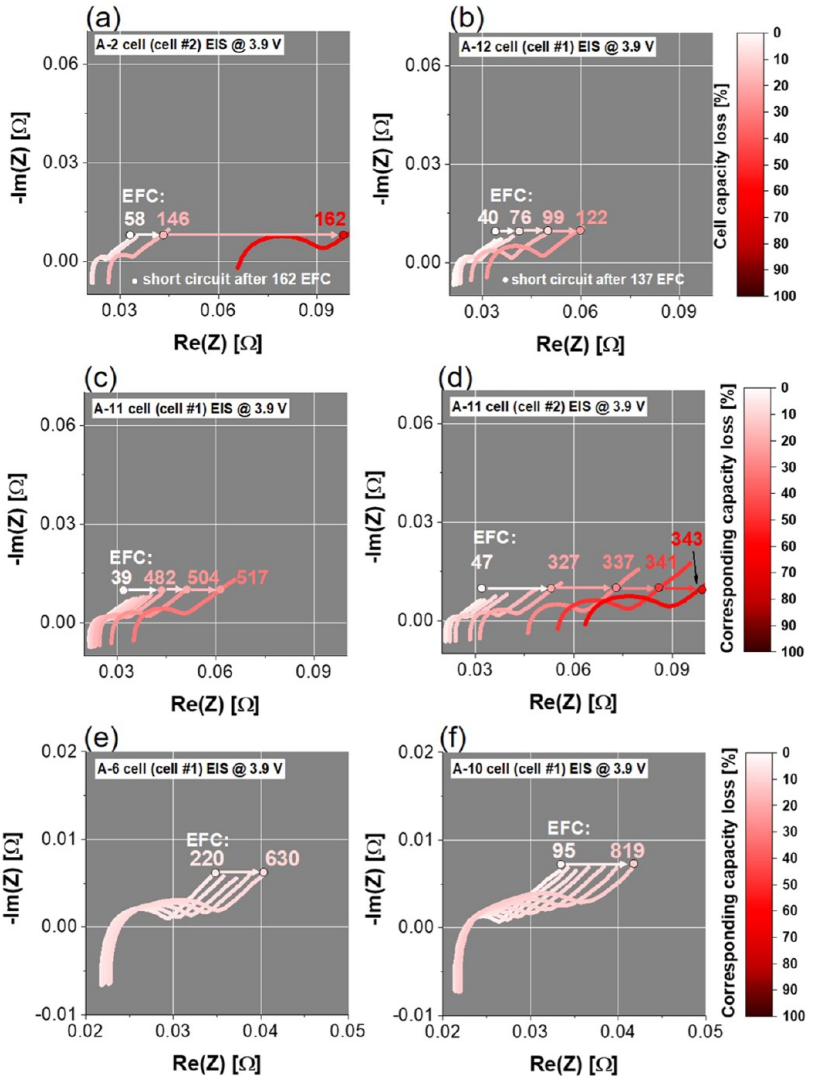

Figure 4. (a–f) Evolution of the EIS at 3.9 V of type *A* cells for selected cycling protocols.

is similar to the *A-6* cells; their R_1 grows faster than R_0. Therefore, it is concluded that the reactions at high voltage dominate the degradation mechanisms for the *A-8* and *A-10* cells, leading to the significant increase of R_1.

A sudden increase of R_0 is observed for highly degraded cells. The increase of the electrolyte decomposition products might not be the only factor influencing R_0. We speculated that the electrolyte shortage (due to severe parasitic reaction) might cause such jumps. To verify this, additional EIS experiments were carried out to examine the effect of electrolyte shortage on R_0.

The experiments were carried out in a half-cell setup consisting of cathode|prewetted Cellgard separator|Li metal. Prewetted separators were prepared by immersing separators in LP30 electrolyte for 4 weeks. Two cells were built; the first was built without additional electrolytes to resemble the electrolyte shortage scenario. For this cell, the prewetted separator serves as the only electrolyte source. The second cell was built with an excess amount of LP30. Because it is difficult to remove one side of the double-sided electrode from cell type *A* without inducing extensive mechanical damage, the cathode for this experiment is taken from cell type *B* that employs a thinner cathode than type *A*. Since this experiment aims to study the influence of electrolyte amount on the relative shift of R_0, the results should still be applicable to explain the sudden jump of R_0 for type *A*.

The influence of the amount of electrolyte on R_0 can immediately be observed after cell assembling; R_0 of the first cell is larger than that of the second cell (see Figure 6a,b). During cycling, R_0 of the first cell increases even more, likely due to parasitic reactions consuming electrolytes. To confirm this, the first cell was opened after 40 cycles and reassembled using a new separator and electrolytes in excess. After reassembling, R_0 decreases (guided by the white arrow in Figure 6a). On the other hand, R_0 of the second cell is constant during cycling because the electrolyte presents in excess since the beginning. Based on this simple experiment, it is concluded that the rapid increase (=jump) of R_0 is primarily induced by the electrolyte shortage, which is further confirmed by conducting postmortem analysis for the *A-1* cell (Section 3.2.2).

It is confirmed that the electrolyte shortage could lead to the jump of R_0. The electrolyte depletion hinders the transport of Li^+ ions between electrodes and eventually prohibits electrochemical reactions.[45] Therefore, it would not be surprising if

https://doi.org/10.1021/acsaem.1c01946
ACS Appl. Energy Mater. 2021, 4, 9982–10002

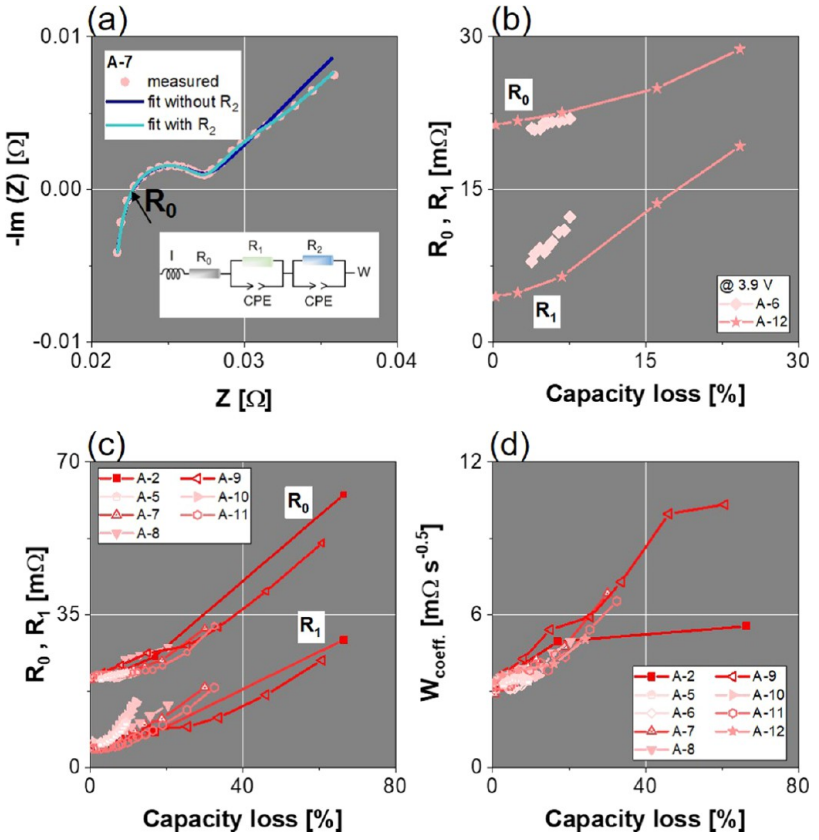

Figure 5. (a) Fitted spectra for the *A-7* cell. Fitted R_0 and R_1 for (b) the *A-6* and *A-12* cells and (c) other cells. (d) Fitted *W*.

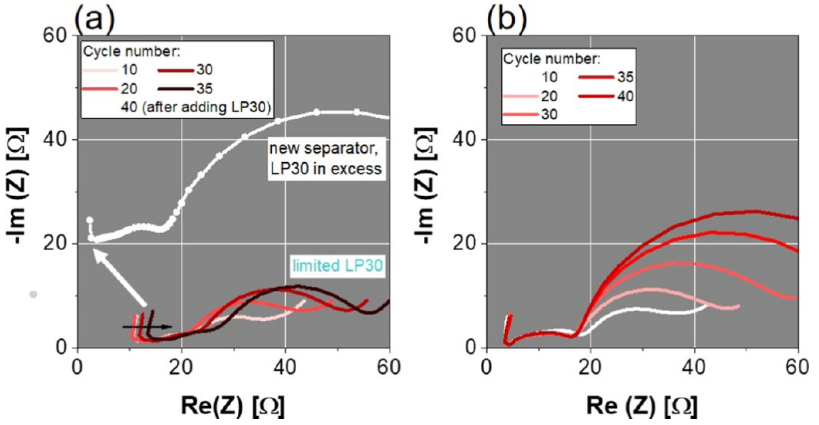

Figure 6. Evolution of the EIS spectra for (a) the first cell, assembled with a limited amount of electrolyte, and (b) the second cell, assembled with an excess of electrolyte (LP30). The EIS spectra were measured at SoC = 8%.

the jump of R_1 observed for highly degraded cells is largely influenced by the electrolyte shortage, too.

Interestingly, the evolution of EIS could also explain the irreproducibility in cell performance. Two cells cycled under the *A-11* protocol serve as suitable examples for this, in which the capacity of the second cell decreases faster than the first one. Figure 4c,d shows that the jump of the R_0, indicating the electrolyte shortage, occurs earlier for the second cell than the first one. Thus, irreproducibility in cell performances is likely related to the remaining electrolyte content during cycling. An et al.[47] reported that a sufficient amount of electrolyte is necessary for long-term cycling stability. It is speculated that long-term cycling stability is also affected by minor inhomogeneity during cell manufacturing, such as tiny differences in an initial amount of electrolytes, particle size distribution, or electrode thickness. In industrial cell production, where the amount of electrolyte is limited to increase energy density and minimize costs, it is actually challenging to attain homogeneous wetting.[48] The spread in the capacity and R_0 (measured at 2.65 V) at BoL for type *A* cells is relatively small, around 1%.

State of health (SoH) of batteries is typically estimated by measuring the remaining capacity or cell impedance. The acquisition time of impedance is relatively faster than measuring the remaining capacity (minutes vs hours). However, the EIS measurement is still considered to be too time-demanding for EV application, and it involves complex calculations to extract relevant parameters.[49−51] The necessity

https://doi.org/10.1021/acsaem.1c01946
ACS Appl. Energy Mater. 2021, 4, 9982−10002

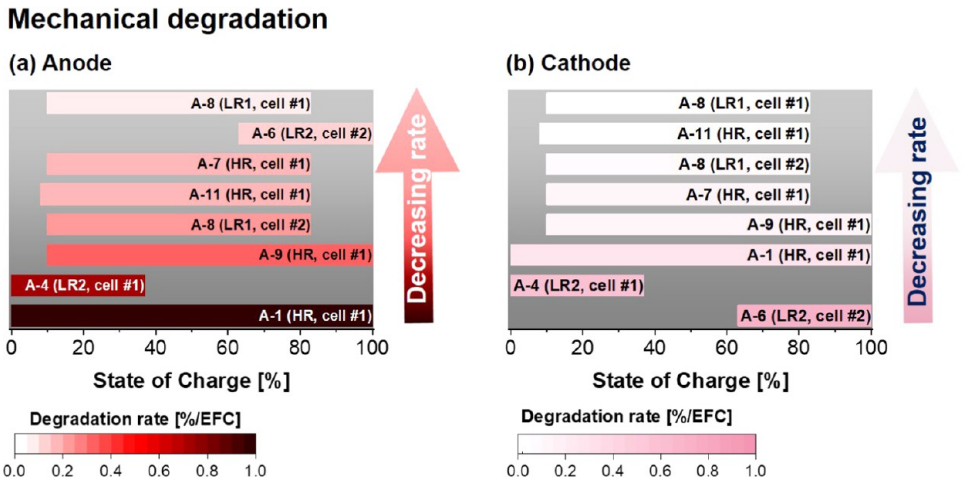

Figure 7. Mechanical degradation of (a) the anode and (b) the cathode of type *A* cells as a function of the state of charge.

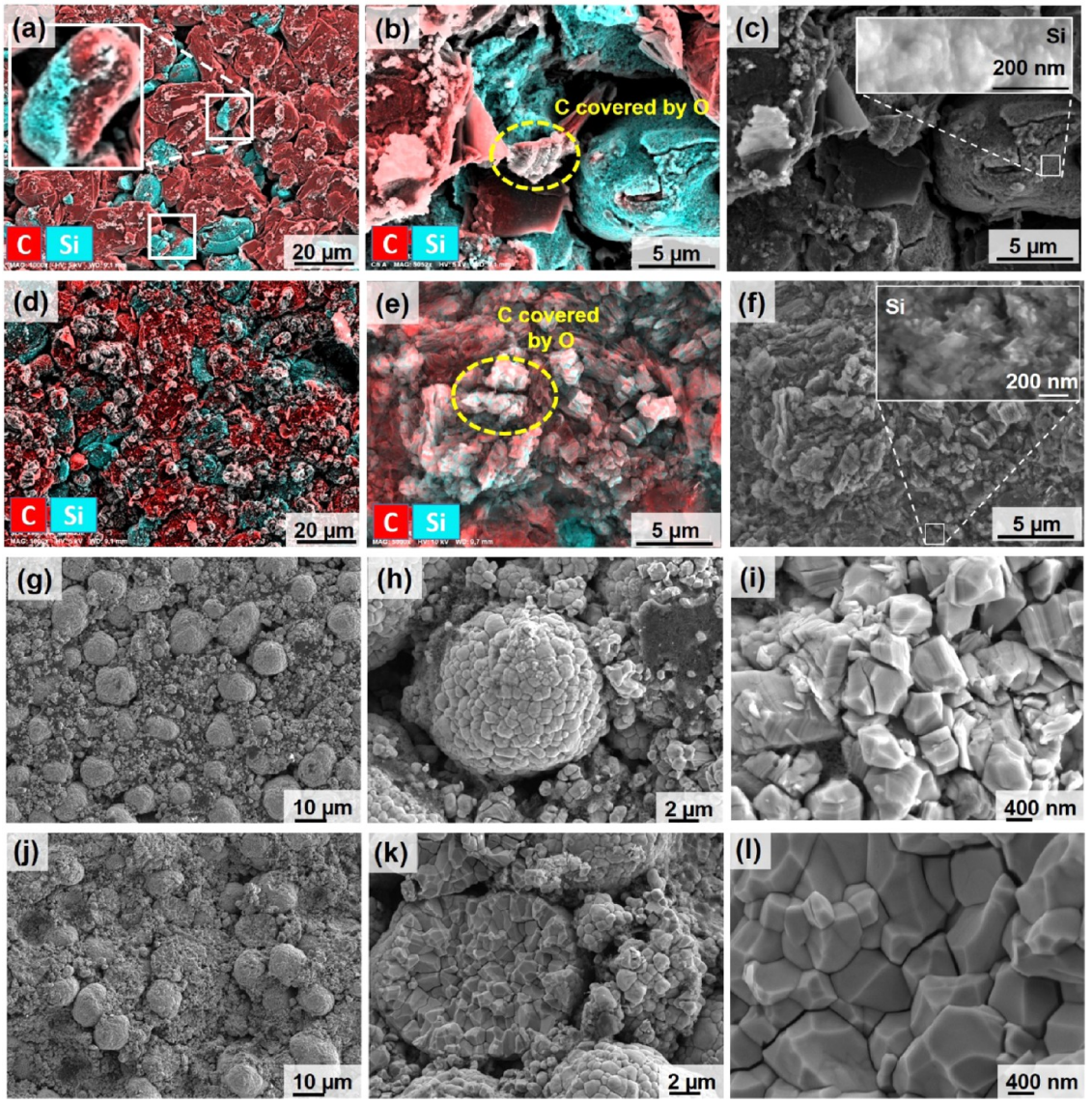

Figure 8. SEM−EDX results of the *A-1* anode at BoL (a−c) and after 252 EFCs (d−f). SEM images of the *A-1* cathode at BoL (g−i) and after 252 EFCs (j−l).

https://doi.org/10.1021/acsaem.1c01946
ACS Appl. Energy Mater. 2021, 4, 9982−10002

to measure a complete EIS spectrum to estimate the SoH is still an open question.[49−51]

Instead of measuring a complete EIS spectrum, it might be sufficient to monitor the increase of R_0. First, the sudden jump of R_0 is a valuable indicator for poor SoH. Second, the evolution of R_0 during cycling shows a weak dependency on the cycling histories. Furthermore, a polynomial fitting correlating the increases of R_0 and capacity losses of all cells results in moderate goodness of fit parameter (see Figure S5); therefore, R_0 can be used to estimate the cell lifetime with reasonable accuracy. Since R_0 is found in the high-frequency region, the acquisition time can be reduced from minutes (complete EIS spectrum) to seconds.

Unlike R_0, R_1 depends strongly on the cycling histories (see Figure 5c); therefore, it is not suitable as an SoH indicator. Furthermore, R_1 overlaps with the Warburg diffusion in the low-frequency region, making it more challenging to interpret and requiring a longer acquisition time than measuring R_0.

3.2. Postmortem Analysis. *3.2.1. Mechanical Degradation.* Mechanical degradation, i.e., material cracking, is deduced from the increase of the BET surface area after cycling, listed in Table S1 for selected cathodes and anodes. The mechanical degradation rate is estimated by dividing the increase of BET surface area by the number of EFCs. Figure 7a,b presents the mechanical degradation of the anodes and the cathodes as a function of the state of charge, respectively.

Except for the *A-6* cell, the anode mechanical degradation rate is larger than its corresponding cathode. For example, the mechanical degradation rate of the *A-1* anode is 0.97%/EFC, while it is 0.27%/EFC for the *A-1* cathode. Interesting results are found for the *A-6* cell: the degradation rate of the *A-6* anode is only 0.14%/EFC (almost the lowest for the cell type *A*), while the degradation rate of the *A-6* cathode is 0.74%/EFC (the highest for the cell type *A*).

By comparing the mechanical degradation of the anode in Figure 7a and of the full cell in Figure 3, it is revealed that mechanical degradation at the anode controls the cell degradation: the higher the (mechanical) degradation rate of the anode, the higher is the degradation rate of the cell. Further investigation by SEM−EDX provides more insight into the phase-specific mechanical degradation of the anode.

Figure 8a−c reveals that the anode of cell type *A* consists of two types of graphite particles, i.e., Si-coated graphite and uncoated ones. A dense agglomeration of spherical nano Si particles is coated on top of some graphite particles, with the size of primary Si particles ranging between 10 and 20 nm.

The mechanical degradation of the anode depends strongly on the lithiation degree of silicon and graphite during cycling. The co-intercalation of "solvated lithium" into graphite between 1 V and 84 mV vs Li^+/Li (corresponds to the cell voltage around 3 V in full cell) might generate additional stress and material exfoliation.[52] Figure 8d−f shows that severe particle fracturing is observed for the *A-1* anode after cycling for 252 EFCs at 100% DoD. The dense agglomeration of the spherical nanosilicon is destroyed and replaced by a porous structure (see the insets in Figure 8c,f). The surface morphology of graphite is significantly modified, with some fraction of graphite being exfoliated from the surface (Figure 8d,e).

Mechanical degradation of the Si particle is expected, driven by the large volume changes of around 400% for full lithiation of silicon.[53] Studies conducted by different groups revealed that degradation of Si-based anodes is mainly associated with the electrochemical activity of $Li_{0.75}Si$ at ∼0.25 V vs Li^+/Li (corresponds to 3.1 V at C/10), causing 110% volume changes.[15,16,38] Those reports also showed that improved cycling stability could be attained by avoiding a complete delithiation of silicon; of course, it is at the expense of reducing cell capacity. It explains that the degradation rates of type *A* cells cycled above 3.1 V are considerably lower than the cells discharged down to 2.65 V.

Even though full lithiation of graphite induces relatively small mechanical stress, i.e., 10% lattice expansion along the *c*-axis and 1% for the *a*-axis,[54] extensive mechanical damage on the graphite particle is found for the cell type *A* cycled at broad DoD, e.g., *A-1* cells. One possible reason is the use of too thick electrodes in high-energy cells, which is detrimental for stress mitigation upon cycling. In contrast to this, the cycling stability of graphite in high-power cells (employing thin electrodes) is reported elsewhere.[55−58] Stiaszny reported that capacity loss of the graphite anode in high-power 18 650 cells (2 Ah) was only 3.7% after 800 cycles, even for the cells cycled at 100% DoD.

Plastic deformation such as fracture occurs when mechanical stress has surpassed its elastic yield. According to the theoretical calculation of finite plastic deformation, the lithium concentration inside a particle is nearly homogeneous when the cycling rate is low, generating low mechanical stress.[25] In contrast to this, the stress gradient inside a particle is more prominent when a higher cycling rate is applied. The center of the particle might have a high stress level that initiates crack propagation when it surpasses yield strength.[23,25] The nonuniform (de)lithiation across the electrode is experimentally evident from either in operando energy-dispersive X-ray diffraction or neutron diffraction experiments.[59,60]

The influence of cycling rate on the mechanical degradation can be studied by comparing, for example, the *A-7* and *A-8* cells. These cells were cycled within the same voltage window but at slightly different rates. The results indicate that cycling rates do not instantly influence cell degradation. As seen in Figure 2d, the capacity losses of the *A-7* (cycled at HR) and *A-8* (cycled at LR1) cells are similar until 250 EFCs. However, the capacity of the *A-7* cells decays faster upon prolonged cycling. In agreement with this, the mechanical degradation rate of the *A-7* anode is higher than that of the *A-8* anode. Crack propagation on the anode is harmful to the cell lifetime because it generates chain reactions, i.e., SEI formation on the new surfaces. The formation of SEI consumes active lithium (and electrolyte) and hence, increases capacity loss.

In contrast to the morphological changes at the *A-1* anode, the surface morphology of the *A-1* cathode does not alter significantly, as seen from the SEM of the cathode at BoL in Figure 8g−i and after 252 EFCs in Figure 8j−l. The morphological change of cathodes likely takes place on a much smaller scale than the spatial resolution of the SEM. Transmission electron microscopy (TEM) studies of fatigued NCA[55] suggest the formation of a NiO-like phase and stacking faults on the surface of degraded NCA, corresponding to a few nanometers of the surface reconstruction layer.

The highest mechanical degradation rate of the cathode is found for the *A-6* cathode cycled between 63 and 100% SoC. This extensive mechanical degradation might be caused by continuous cycling around the maximum lattice parameter *c* at ∼4.08 V vs Li^+/Li (see Section 3.2.4). A large mechanical degradation rate is also found for the *A-4* cathode, cycled between 0 and 37% SoC. Surprisingly, this mechanical degradation of the *A-4* cathode is even larger than the *A-1*

https://doi.org/10.1021/acsaem.1c01946
ACS Appl. Energy Mater. 2021, 4, 9982−10002

cathode cycled at 100% DOD. The reason for this remains unclear.

3.2.2. Electrochemical Characterization of Cathode, Anode, and Full Cell. The electrochemical characterizations were carried out for the BoL and the *A-1* cell after 137 EFCs and 252 EFCs. Before the electrochemical characterizations of cathode, anode, and full cell, one side of the double-sided electrode was removed by DMC. This electrode preparation induces additional mechanical damage to the electrodes; therefore, the capacities measured after cell opening are typically lower than before cell opening.

The capacities of the full cells measured before and after cell opening are given in Table 4. Note that the full cell capacity is normalized to the total area of the cathode. A slight discrepancy in capacity before and after cell opening at BoL and after 137 EFCs can be attributed to the electrode preparation. However, a surprising result is shown for the *A-1* cell after 252 EFCs, with the capacity measured after cell opening being significantly higher than before cell opening (3.24 vs 0.19 mAh/cm^2). This large discrepancy cannot be associated with electrode preparation. The "new" electrolyte (amount) might explain this huge discrepancy. As indicated by the impedance jump in Figure S4a, the electrolyte shortage before opening the *A-1* cell caused a considerable capacity loss.

Table 4. Full-Cell Capacities Measured before and after the Opening of the *A-1* Cells at BoL, after 137 EFCs, and after 252 EFCs

	capacity (mAh/cm^2) at a rate of C/10	
cell	before cell opening	after cell opening
A cell (BoL)	4.59	4.54 ± 0.02
A-1 cell (cycled for 137 EFCs)	4.21	3.99 ± 0.11
A-1 cell (cycled for 252 EFCs)	0.19	3.24 ± 0.20

In contrast to this, fresh electrolytes in a generous amount are used after cell opening; therefore, the capacity of the *A-1* cell can be partially regained.

The capacity losses of the cathode and anode were estimated by the galvanostatic method. The cathode was cycled against lithium between 3.0 and 4.25 V, while the anode was cycled between 10 mV and 2.0 V. The capacity losses are then determined from the difference between the capacity of the fatigued electrodes relative to its initial capacity at BoL (summarized in Figure 9a).

For postmortem analysis, all of the cells were opened in a fully discharged state at 2.65 V. Therefore, almost all of the active lithium is found in the as opened cathode at BoL. However, a substantial amount of lithium can be found in the as opened degraded anode, even though the degraded cell was opened at 2.65 V. To estimate the remaining active lithium, the as opened cathode is charged against lithium to 4.25 V at C/10 (Figure 9b). At the same time, the as opened anode is discharged against lithium to 2.0 V (Figure 9c). The sum of the charging capacity of the cathode and the discharging capacity of the anode correlates to the amount of active lithium inside full cells (see Figure 9b–d). The lithium loss is then estimated from the difference between lithium amount at BoL and fatigued states (summarized in Figure 9a). The losses of lithium, cathode, and anode in the *A-1* cell are similar for the first 137 EFCs. Afterward, lithium and cathode losses grow faster than the anode loss.

3.2.3. Immobilized Lithium in the Degraded Anode. As evident from the galvanostatic cycling, a considerable amount of lithium is stored in the as opened degraded anode even when the (degraded) cell was opened at 2.65 V. The lithium can be stored in the degraded anode as Li-plating or immobilized lithiated graphite. The lithiated graphite phases are even visible from its distinct colors (dark black-blue: graphite, red-brown: LiC_{12}, and gold yellowish: LiC_6).

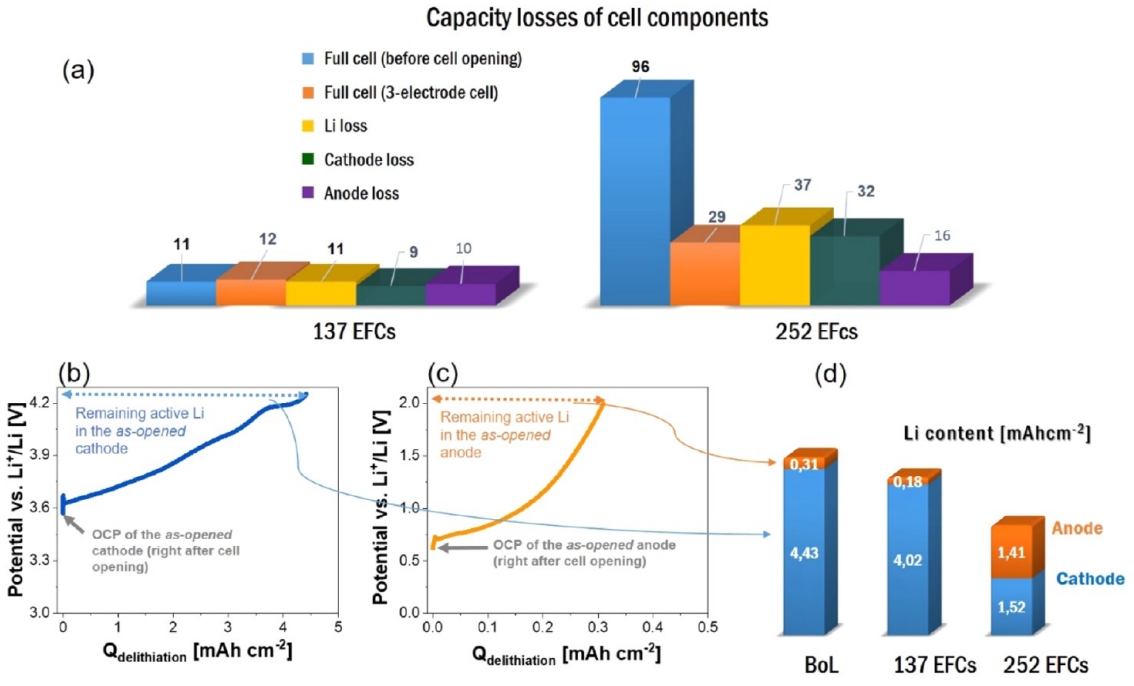

Figure 9. (a) Capacity losses of the full cell (before and after cell opening), active lithium, cathode, and anode of the *A-1* cell after 137 EFCs and 252 EFCs. Potential profiles at (b) the first charge of cathode vs lithium and (c) the first discharge of anode vs lithium. (d) Lithium amount in the *A-1* cell at BoL, after 137 EFCs, and after 252 EFCs.

https://doi.org/10.1021/acsaem.1c01946
ACS Appl. Energy Mater. 2021, 4, 9982−10002

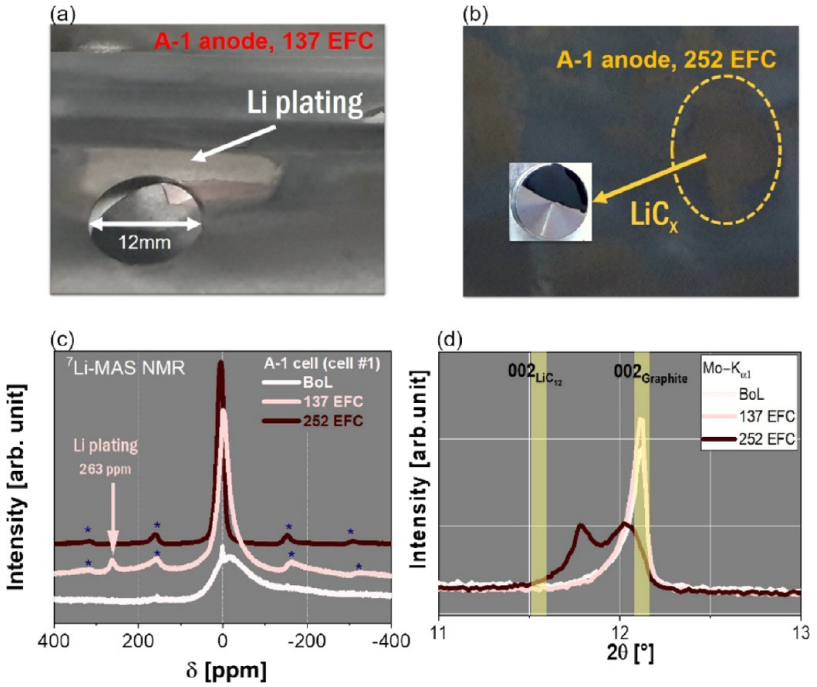

Figure 10. As opened anode: (a) Li plating is observed on the surface of the anode after 137 EFCs. (b) Lithiated graphite is indicated from the yellowish-gold color on the surface anode after 252 EFCs. Li platting is confirmed from (c) NMR, while the lithiated graphite phase is confirmed from (c) NMR and (d) XRD of the as opened anode.

In fact, Li-plating is observed in the *A-1* cell after 137 EFCs, which is easily identified visually from glossy silverish fragments on the anode surface as shown in Figure 10a and further confirmed from analytical investigation ^{7}Li-MAS NMR.

Interestingly, a large area of Li plating is not found on the anode surface of the *A-1* cell after 252 EFCs. One possible explanation is that Li-plating and Li-striping are (partially) reversible. Alternatively, the lithium plating is localized at tiny spots that cannot be observed with bare eyes. Instead of Li-plating, a lithiated graphite phase is observed on the as opened *A-1* anode after 252 EFCs (see Figure 10b).

Figure 10c shows ^{7}Li-MAS NMR revealing a chemical shift associated with Li metal at around 263 ppm for the *A-1* cell after 137 EFCs. The ^{7}Li MAS NMR spectra of the BoL anode exhibit a broad peak centered at around −12 ppm, associated with a mixture of ionic lithium in the SEI and in the electrolyte.[61] The signal of random distribution of a small amount of remaining lithium in graphite might also be integrated into this broad peak.[61,62] For the *A-1* anode after 252 EFCs, the main peak shifts to a positive value of around 6 ppm, indicating the existence of a lithiated graphite phase (LiC_x). The peaks marked with asterisks represent the spinning side bands of the main peak. The LiC_x phase is further confirmed from XRD as presented in Figure 10d, suggesting the coexistence of graphite and LiC_x ($x > 12$) phases for the as opened *A-1* anode after 252 EFCs.

3.2.4. In Operando XRD. In operando XRD patterns of the BoL cathode are presented in Figure 11a. The cathode is cycled against lithium metal between 3.0 and 4.25 V. All cathode reflections can be indexed with the $R\bar{3}m$ space group, as indicated in blue by the *hkl* in Figure 11a.

XRD analysis reveals that the lithium concentration is not uniform upon cycling above 3.85 V. When two fractions of particles coexist, two sets of lattice parameters (a_1, c_1) and (a_2, c_2) are refined. The goodness-of-fit parameter improves when a structural model based on nonuniform (de)lithiation is considered; the examples for refined XRD patterns are given in Figure S7.

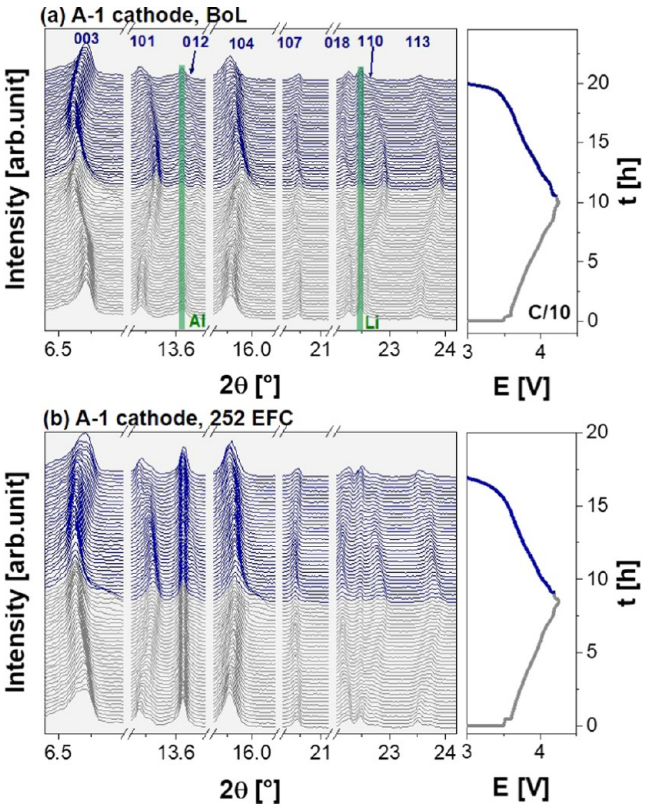

Figure 11. In operando XRD patterns of the *A-1* cathode (a) at BoL and (b) after 252 EFCs.

https://doi.org/10.1021/acsaem.1c01946
ACS Appl. Energy Mater. 2021, 4, 9982−10002

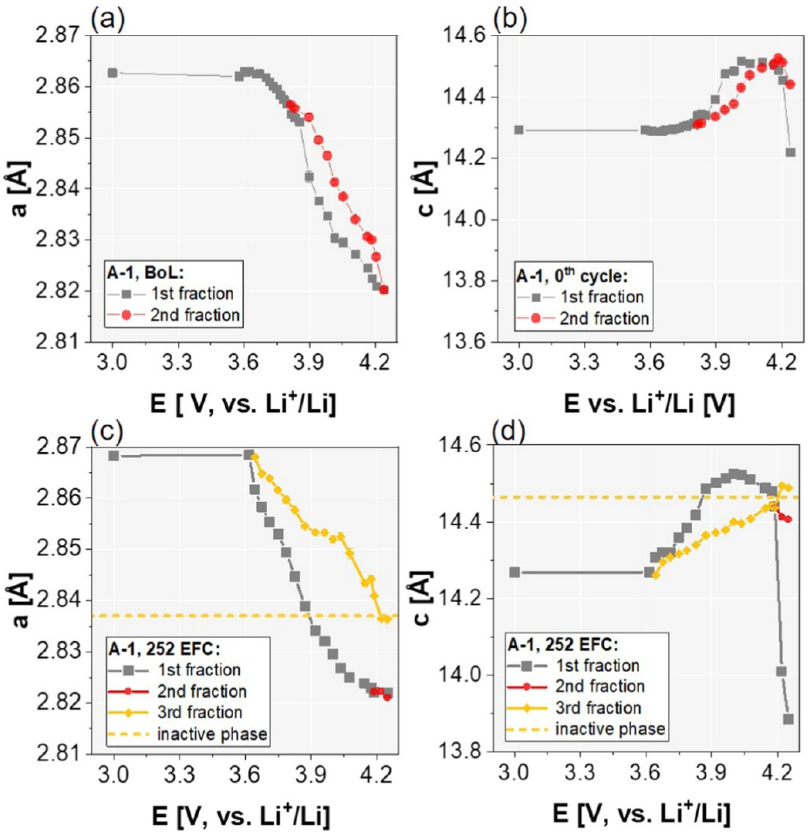

Figure 12. Lattice parameters *a* and *c* for the *A-1* cathode at (a, b) BoL and (c, d) after 252 EFCs.

Table 5. Elemental Analysis of Cathode and Anode of the 3.5 Ah Cells for the BoL and the *A-1* Cell at Different EFC Numbers

	cathode (wt %)			anode (wt %)		
		A-1 cathode			*A-1* anode	
element	BoL	137th EFC	252nd EFC	BoL	137th EFC	252nd EFC
Li	5.79 ± 0.01	5.50 ± 0.01	3.45 ± 0.02	1.73 ± 0.03	2.37 ± 0.02	5.03 ± 0.07
O	30.50 ± 0.40	30.70 ± 0.7	30.6 ± 1.1	6.54 ± 0.21	7.77 ± 0.24	16.8 ± 0.4
Al	0.38 ± 0.01	0.38 ± 0.06	0.41 ± 0.011	0.0015 ± 0.0002	0.0019 ± 0.0001	0.0015 ± 0.0003
Co	6.10 ± 0.03	6.19 ± 0.04	6.32 ± 0.05	0.0006 ± 0.0002	0.0015 ± 0.0001	0.0031 ± 0.0001
Ni	48.70 ± 0.04	49.20 ± 0.05	50.24 ± 0.15	0.0042 ± 0.0019	0.0072 ± 0.0001	0.0123 ± 0.0002
Si	not analyzed			1.76 ± 0.02	1.71 ± 0.03	1.57 ± 0.03
total (wt %)	91.05	91.97	91.02	10.0365	11.8604	23.4169

The refined lattice parameters for the BoL cathode during cycling are presented in Figure 12a,b. The lattice parameter *a* contracts gradually during delithiation due to the shrinking of the transition metal (TM)−oxygen bonds in TMO_6 octahedra.[63] The corresponding lattice parameter *c* expands during charging to 4.08 V. The expansion of *c* is associated with the electrostatic repulsion of two neighboring oxygen layers.[63] The oxygen is then partially oxidized above 4.08 V, compensating for this repulsion. Therefore, the lattice parameter *c* decreases upon further charging.

The most interesting behavior is observed at the end of charge at 4.25 V, with the lattice parameters *a* of the first and second fractions similar to each other (Figure 12a); however, their corresponding lattice parameters *c* differ considerably. The lattice parameter *c* of the first fraction (~20 wt %) is significantly lower than the second one; it is even smaller than that at discharged state at 3.0 V.

In operando XRD experiments were also performed for the *A-1* cathode after 252 EFCs (presented in Figure 11b). It is found that the fatigued cathode contains the same phase as for the BoL one. However, some fractions of NCA become inactive and hence do not participate in the (de)lithiation any longer. The structural refinement reveals that 27 wt % NCA becomes inactive after cycling.

Lattice parameters *a* and *c* of the fatigued cathode are shown in Figure 12c,d. The lattice parameters of the inactive phase are constant during cycling, indicated as dashed yellow lines. The contraction of lattice parameter *c* between 4.03 and 4.25 V is larger for the cathode after 252 EFCs than that at BoL. This larger compression stress in the degraded cathode might accelerate mechanical degradation.

One of the mechanisms for cathode loss is the dissolution of Ni and Co from the cathode and then deposited on the anode.[27−29] The elemental analysis by ICP−OES (Table 5) confirms this mechanism, where the weight percentage of Ni and Co increases for the fatigued anodes. Both Ni and Co are already present at the BoL anode, indicating that these active elements might already be dissolved during storage (calendric

https://doi.org/10.1021/acsaem.1c01946
ACS Appl. Energy Mater. 2021, 4, 9982−10002

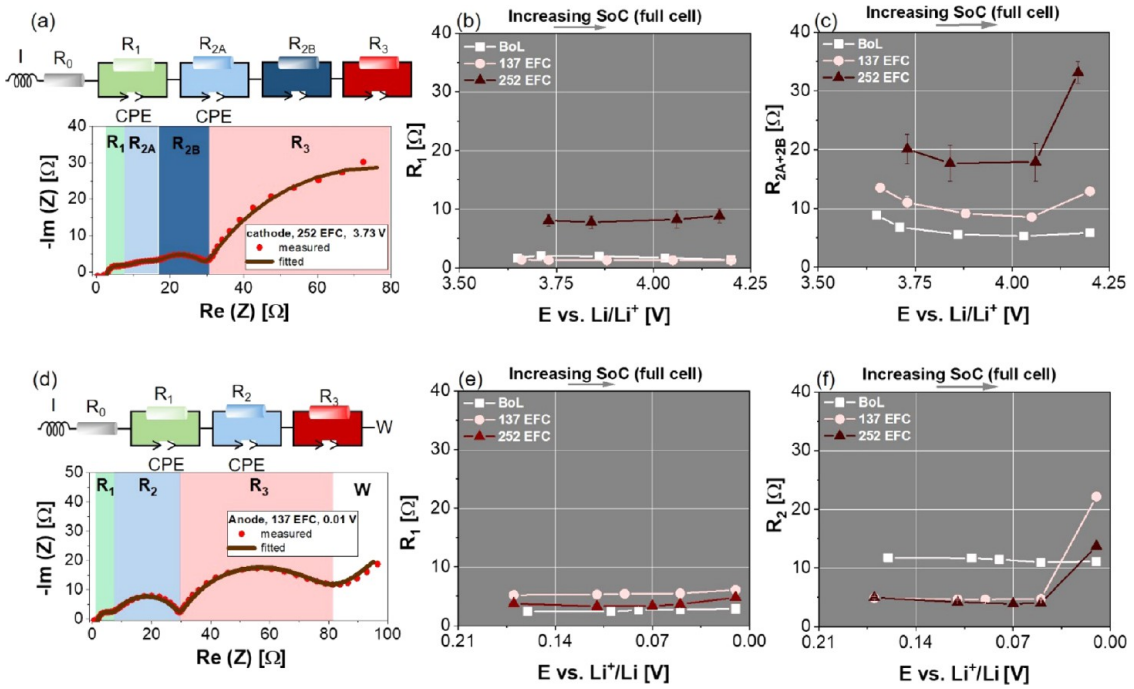

Figure 13. Equivalent circuit models to fit the EIS spectra of (a) the *A-1* cathode and (d) the *A-1* anode. The examples of fitted spectra are given for the cathode after 252 EFCs and for the anode after 137 EFCs. The fitted impedance is presented in (b) and (c) for the cathode and (e) and (f) for the anode, respectively.

aging) before the cycling test. It is speculated that the deposited transition metal on graphite anode accelerates side reactions by increasing the average electronic conductivity of the SEI layer.[29] Faenza et al. proposed that dissolved transition-metal ions are reduced on the anode (forming metal), promoting catalytic reactions.[6]

3.2.5. EIS of Cathodes and Anodes Taken from the 18650 Cells of Type A. The Nyquist diagrams of the *A-1* electrodes (cathode and anode) at BoL, after 137 EFCs, and after 252 EFCs are presented in Figure S8. The equivalent circuit models (ECMs) to fit those spectra for the cathode and the anode are shown in Figure 13a,d, respectively. The fitted spectra for the *A-1* cathode after 252 EFCs and the *A-1* anode after 137 EFCs are shown below the ECM. The evolution of the polarization impedance is given as a function of potential in Figure 13b,c,e,f. The x-axis for anode potential (Figure 13e,f) is given in a reversed order to resemble the evolution of anode potential during charge in a full cell.

For the cathode, R_1 is probably associated with the contact resistance between the current collector and active materials.[46] Two semicircles, labeled as R_{2A} and R_{2B}, are observed in the high- to medium-frequency region. The in operando XRD suggests that the lithium concentration is not uniform during cycling (the most pronounced evidence is found at 4.2 V), leading to a local variation of the state of charge. Since the charge transfer resistance depends strongly on the state of charge, it is speculated that R_{2A} and R_{2B} are partially influenced by the coexistence of two or more fractions of particles having slightly different lithium concentrations. Additionally, the R_{2A} might also be affected by the transport resistance through the CEI. Since R_{2A} and R_{2B} cannot be resolved for some spectra due to the strong overlapping of these two types of resistances, only the sum of R_{2A} and R_{2B} is presented in Figure 13c. For the anode, R_1 is interpreted as a mixture of contact resistance and transport resistance through SEI, while R_2 is correlated to the charge transfer resistance. For both cathode and anode, a semicircle in the low-frequency region is modeled as R_3. For most cases, R_3 appears as an incomplete semicircle (see the spectra in Figure S8). In this frequency region, several processes might co-occur, including Warburg diffusion and ion transport in pores.[1,45,46] Due to its complexity, the impedance in the low-frequency region is not discussed in this manuscript.

At BoL, the charge transfer resistance (R_{2A} + R_{2B}) of the cathode is smaller than the anode, but it increases significantly during cycling. In contrast to this, the charge transfer resistance of the anode declines, except at 10 mV vs Li^+/Li (corresponding to 100% SoC in full cells). The impedance of the *A-1* anode is even smaller than the cathode after 252 EFCs. It suggests that the cathode controls the reaction kinetics in the degraded cells. The decrease in the impedance of the degraded anodes is reported in ref 46.

It is shown here that the contact resistance of Al current collector−cathode material (R_1) is nearly constant for the first 137 EFCs, but it increases afterward. On the other hand, the sum of R_{2A} and R_{2B} increases continuously during cycling. In contrast, the charge transfer resistance of the anode decreases during cycling, except for the charge transfer resistance at 0.01 V. The highest R_1 (likely dominated by the SEI resistance) is found for the *A-1* anode after 137 EFCs. Surprisingly, it decreases on further cycling up to 252 EFCs. This decrease might indicate partial dissolution of SEI at the end of the 252nd EFC.

The largest increase of charge transfer resistance is found at around 4.2 V (vs Li^+/Li) for the cathode and at 0.01 V (vs Li^+/Li) for the anode. It suggests that kinetics for electrochemical reactions becomes extremely difficult for the fatigued cells at high SoC and explains that the inactive fraction of the *A-1* cathode is in a partially lithiated state.

https://doi.org/10.1021/acsaem.1c01946
ACS Appl. Energy Mater. 2021, 4, 9982−10002

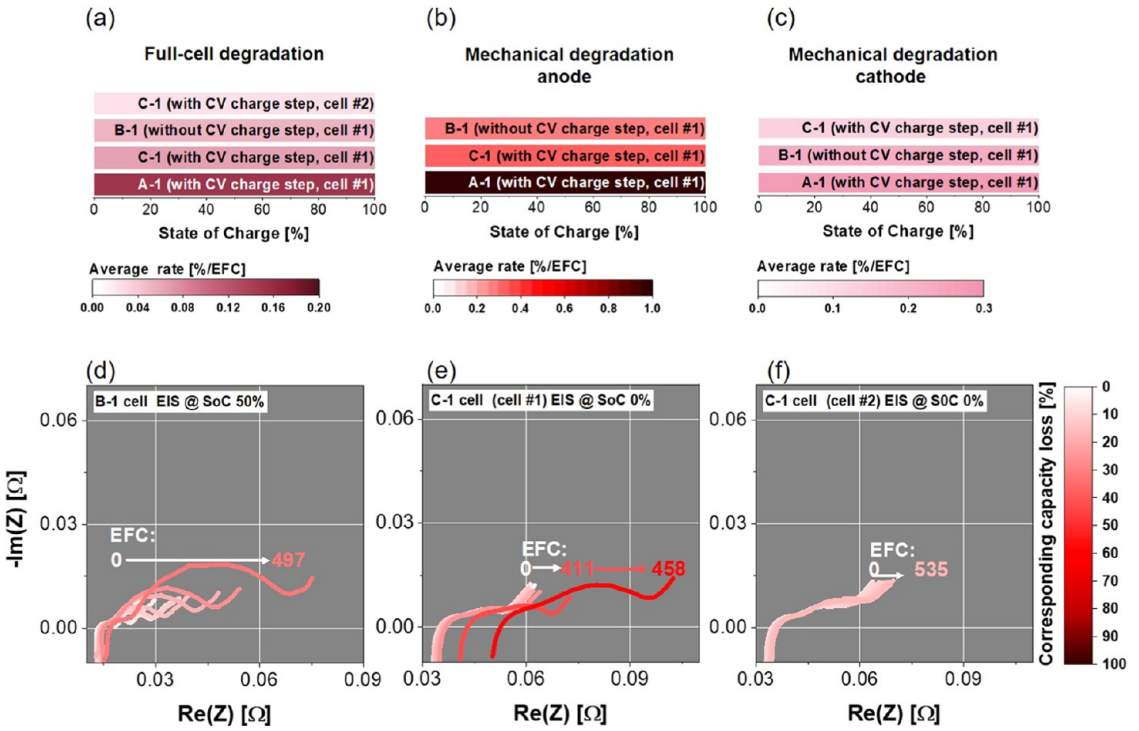

Figure 14. (a) Degradation rates of the *A-1*, *B-1*, and *C-1* cells. Mechanical degradation rates of the corresponding (b) anodes and (c) cathodes. The evolution of the EIS spectra for the (d) *B-1* cell,[7] (e) *C-1* cell (cell #1), and (f) *C-1* cell (cell #2).

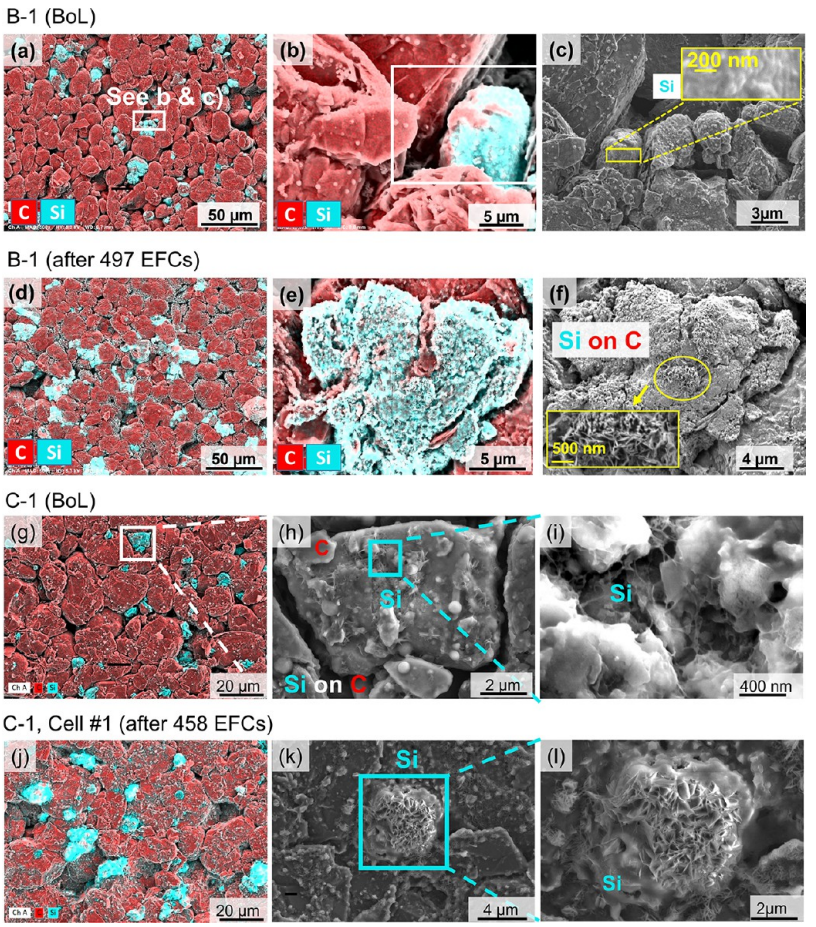

Figure 15. (a) SEM–EDX images of the *B-1* anode (a–c) at BoL and (d–f) after 497 EFCs. SEM–EDX images of the *C-1* anode (g–i) at BoL and (j–l) after 458 EFCs.

https://doi.org/10.1021/acsaem.1c01946
ACS Appl. Energy Mater. 2021, 4, 9982–10002

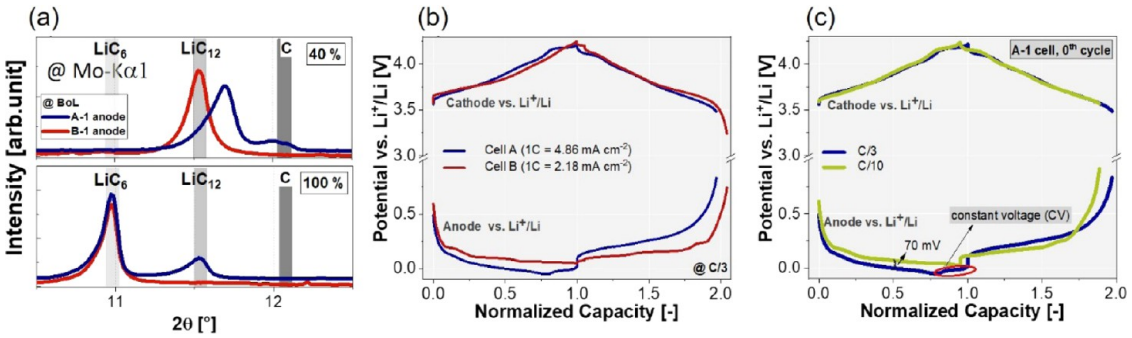

Figure 16. (a) XRD patterns for the A-1 and B-1 anodes at BoL. Anode and cathode potential profiles at BoL as a function of (b) electrode thickness and (c) current. The measured capacities are normalized to the amount of charge capacity.

4. DISCUSSION

4.1. Influence of Cell Design on Cell Degradation. The influence of the electrode thickness, particle size, and electrode architecture on the cell performance is discussed by comparing the performance of the *A-1* cells with other two 18 650 cells employing similar electrode chemistries, labeled as the *B-1* and *C-1* cells. They were cycled at 100% DoD and at a charge−discharge rate of 1C−1C for the *B-1* cell and C/2−1C for the *C-1* cell. The cycling performances of the *B-1* and *C-1* cells are summarized in Figure 14a−c, with the average degradation rates calculated using the same procedure as for the *A-1* cell. The impedances of the *B-1*[7] and *C-1* cells are presented in Figure 14d−f, with color progression correlating the cell impedance to the capacity loss.

The capacity losses of the *B-1* and *C-1* cells are given in Figure S9. The capacity losses of the cathode, anode, and active lithium for the *B-1* cell after 497 EFCs are presented in Figure S10. The cathode and anode sheets of the *C-1* cells are exfoliated from their current collectors after cycling for more than 450 EFCs; therefore, it is impossible to perform electrochemical characterization for these electrodes.

Among the three cell types (*A*, *B*, *C*) cycled under a similar cycling protocol, the *A-1* cell degrades the fastest (Figure 14a). The *C-1* cell (cell #1) degrades more rapidly than the *B-1* cell (Figure 14a,b). At the same time, the mechanical degradation rate of the *C-1* anode is higher than the *B-1* anode. It suggests that the performances of cell types *B* and *C* depend strongly on the degradation degree of its anodes, which is also observed for cell type *A*.

Unlike the *A-1* cell, the large jump of R_0 was not observed for the *B-1* cell (Figure 14d). Therefore, it is concluded that the drying out of electrolytes has not yet occurred in this cell. The electrolyte shortage is only observed for one of the two cells cycled under the *C-1* protocol (Figure 14e, cell #1). Therefore, a fast capacity decay is observed for this cell and not for the second *C-1* cell.

Cell types *A* and *B* employ the same type of anode materials, i.e., Si-coated graphite and noncoated graphite. The morphology of Si coating is the same for the two cells, i.e., agglomeration of spherical nano Si on the graphite particle. However, their mechanical degradation rates differ significantly. The SEM−EDX examinations suggest that the Si particles of the *A-1* and *B-1* anodes are partially exfoliated from the graphite substrate during cycling (Figures 8d−f and 15d−f). However, the degradation degree of its graphite is not the same, with the graphite particles of the *A-1* anode degrading more severely than for the *B-1* anode.

The main differences between the *A-1* and *B-1* anodes are the particle size and electrode thickness. The BET surface area of the *A-1* anode at BoL is significantly smaller than that of the *B-1* anode (1.76 vs 3.08 m^2/g), suggesting that the average particle size of the *A-1* anode is larger than that of the *B-1* anode. For the same type of material, crack propagation gets more severe for larger particles,[22,24] explaining partially that the mechanical degradation rate is higher for the *A-1* anode than for the *B-1* anode.

The *A-1* anode is roughly 2 times thicker than the *B-1* anode. Ex situ XRD examines the influence of electrode thickness on the lithiation process. The ex situ XRD reveals that the phase composition of the *A-1* and *B-1* anodes at the same SoC is not always identical, even when they were lithiated at a slow rate of C/10 (Figure 16a). At 40% SoC, all graphite is transformed into LiC_{12} for the thinner anode (from cell type *B*). However, it is not the case for the thicker one (from the cell type *A*). At 100% SoC, the thinner anode is fully lithiated, while the thicker anode consists of a mixture of LiC_{12} and LiC_6. Since the strain−stress profile is influenced by the type of phase that exists on the particle surface and the ratio of the coexisting phases,[24,41,64] it is not surprising that the mechanical degradation rate for the *A-1* differs from the *B-1* anodes.

The electrode thickness affects not only the lithiation kinetics but also cell safety. Figure 16b compares potential curves of the positive and negative electrodes of cell types *A* and *B* during cycling at a rate of C/3 employing a three-electrode cell. The potential of the thicker anode (*A-1* cell) drops very fast to subzero volt, forming Li-plating. The lithium plating is observed as silverish stripes on the anode surface of the *A-1* cell after 137 EFCs (Figure 10a). As shown in Figure 16c, high-energy cells have to be cycled at a lower rate to avoid lithium plating. Another alternative to avoid lithium plating is by lowering the upper voltage limit at the expense of a smaller capacity. Thus, the goal of the high-energy-density LIBs is limited by the safety aspect.

Cell types *A* and *C* are classified as high-energy cells; hence, their electrode thickness is comparable. Even though both cells were cycled under the same cycling protocol, their cycling stability differs. The cycling performance of the *C-1* cell is better than that of the *A-1* cell, partly because cycling-induced mechanical degradation is slower for the *C-1* anode than for the *A-1* anode.

Both consist of the same type of anode materials, i.e., Si-coated graphite and uncoated graphite (Si ∼2 wt %). The SEM−EDX examination shown in Figure 15g−i reveals that the silicon coating on graphite of the *C-1* cell exhibits a porous

https://doi.org/10.1021/acsaem.1c01946
ACS Appl. Energy Mater. 2021, 4, 9982−10002

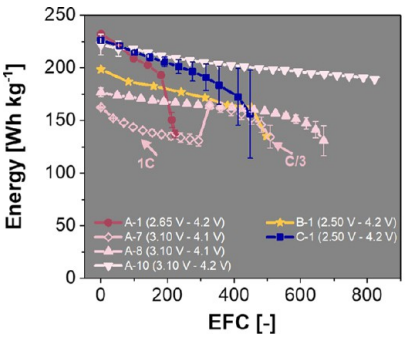

Cell id	Cost-per-wear [€/kWh]	Power [W]	Remarks
A-1	4.18 +/- 0.20	11.8	--
A-7	1.46 +/- 0.08	12.2*	*1st – 500th cycle
		4.2**	** After 500th cycle
A-8	1.10 +/- 0.10 *	4.2	*Cap loss 16 % +/- 4%
A-10	0.92 +/- 0.01 *	4.2	*Cap. loss 11 % +/- 1 %
B-1	1.81	9.0	Estimated from [7]
C-1	1.2 +/- 0.4	12.0	

Figure 17. Figure of merit of three types of 18650 cells, labeled as cell types *A*, *B*, and *C*. The cost per wear is calculated based on the price of a new cell divided by the total energy throughput during its lifetime (buying price of cell type *A*: €8.76, buying price of cell type *B*: €7.79, buying price of cell type *C*: €7.09).

structure resembling a spider-like network, which is in contrast to the dense agglomeration of spherical nano Si for the *A-1* anode. It seems that this porous architecture mitigates partially cycling-induced mechanical stress in the *C-1* anode so that, as observed in Figure 15j–l, crack propagation occurs only for silicon. The crack is not observed for the graphite particles for the *C-1* anode, which contrasts with the *A-1* anode.

The SEM–EDX examination and the estimated mechanical degradation by the BET surface area for cell types *A*, *B*, and *C* suggest that mechanical degradation of the anode and, consequently, electrolyte consumption could be controlled by employing suitable particle architecture thinner electrodes.

4.2. Figure of Merit: A Balance between Energy Density, Power Density, and Cost per Wear. For EV applications, high energy and power density are essential to fulfill the demands for a longer travel distance at a reasonable rate. Another crucial criterion is a long life span to minimize the cost per wear. The cost per wear is calculated from the price of a new cell divided by the total energy throughput during its lifetime before reaching EoL, except for the *A-8* and *A-11* cells. For the latter, the average capacity losses are still less than 20%. Figure 17 compares the overall performances of the cells of types *A*, *B*, and *C* evaluated based on their energy density, power, and cost per wear.

It is shown here that the cost per wear of the *A-1* cells depends strongly on cycling protocols: it ranges from €0.9/kWh for the *A-10* protocol to €4.1/kWh for the *A-1* protocol. These results highlight the importance of using an optimum cycling protocol. The costs per wear of the *B-1* and *C-1* cells are in between these margins. If the cycling stability of the *C-1* cell (cell #2) were reproducible, this cell type would outperform the cells of types *A* and *B* from all aspects: power, energy, and cost per wear.

5. SUMMARY

It is identified for type *A* cells (3.5 Ah, 18 650, NCAlC/Si) that mechanical degradation (fracture) of the active materials, graphite, and Si, is one of the primary mechanisms for cell failure as it initiates extensive electrolyte consumption. The mechanical degradation rate could be lowered by narrowing the depth of discharge and avoiding cycling at a low operating window to suppress the electrochemical activation of $Li_{0.75}Si$.

At the beginning of the cycling, the degradation rate increases linearly as a function of EFC. Within this linear regime, electrolyte consumption is mainly driven by the cycling-induced fracture of the SEI layer. Therefore, the rate of capacity loss is pretty low. Long-term cycling generates fracture of active materials and SEI, increasing rapidly the electrolyte consumption rate used for SEI formation on new particle surfaces. When the amount of electrolyte is no longer sufficient for Li^+ transport from cathode to anode and vice versa, the ohmic resistance (R_0 in EIS spectra), and capacity loss (even at C/25) of the cell escalate.

The rate of mechanical degradation of anode materials is lower for high-power cells using thinner electrodes (cell *B*). This rate could also be lowered by employing particles with smaller sizes and porous Si nanoparticles (cell *C*). During industrial cell manufacturing, the initial electrolyte amount is typically scaled with the total pore volumes of cathode, anode, and separator. The studies conducted here suggest that the rate of cycling-induced mechanical degradation of active material shall also be considered in calculating the initial amount of electrolyte, especially for the cells employing thicker electrodes.

For type *A* cells, the electrode thickness of commercial LIBs is doubled to increase the energy density. However, the electrode thickness cannot be increased infinitely, not only because it decreases the rate capability and accelerates the active material fracture but also because it lowers the cell safety. Due to the large overpotential found for thicker electrodes, lithium plating is more prevalent for cell type *A* than for cell type *B*. Furthermore, the capacity of the thicker anode is partially inaccessible, even at a very slow rate of C/10, which is against the main goal to increase the energy density.

As an outlook, operando neutron powder diffraction (NPD) data will provide a clearer picture of the different fatigue states. As such, the NPD measurements are planned for the near future within the project of the "Energy research with Neutrons (ErwiN)" project at MLZ.[65]

■ ASSOCIATED CONTENT

Supporting Information

The Supporting Information is available free of charge at https://pubs.acs.org/doi/10.1021/acsaem.1c01946.

Additional experimental results of differential capacity plots, voltage profiles, impedance spectra, SEM–EDX, XRD, capacity loss comparison of the *A-1*, *B-1*, and *C-1* cells, and BET surface area (PDF)

■ AUTHOR INFORMATION

Corresponding Author

Mariyam Susana Dewi Darma – *Institute for Applied Materials (IAM), Karlsruhe Institute of Technology (KIT),*

https://doi.org/10.1021/acsaem.1c01946
ACS Appl. Energy Mater. 2021, 4, 9982–10002

76344 Eggenstein-Leopoldshafen, Germany; Helmholtz Institute Ulm (HIU) Electrochemical Energy Storage, 89081 Ulm, Germany; orcid.org/0000-0002-1711-4499; Email: susana.darma@battronics.com, darma.mariyam@gmail.com

Authors

Jiangong Zhu − *Institute for Applied Materials (IAM), Karlsruhe Institute of Technology (KIT), 76344 Eggenstein-Leopoldshafen, Germany*

Peng Yan − *Institute for Applied Materials (IAM), Karlsruhe Institute of Technology (KIT), 76344 Eggenstein-Leopoldshafen, Germany*

Chenghao Zheng − *Institute for Applied Materials (IAM), Karlsruhe Institute of Technology (KIT), 76344 Eggenstein-Leopoldshafen, Germany*

Martin J. Mühlbauer − *Institute for Applied Materials (IAM), Karlsruhe Institute of Technology (KIT), 76344 Eggenstein-Leopoldshafen, Germany; Heinz Maier-Leibnitz Zentrum (MLZ), Technische Universität München, 85748 Garching, Germany*

Daniel R. Sørensen − *Heinz Maier-Leibnitz Zentrum (MLZ), Technische Universität München, 85748 Garching, Germany*

Sylvio Indris − *Institute for Applied Materials (IAM), Karlsruhe Institute of Technology (KIT), 76344 Eggenstein-Leopoldshafen, Germany;* orcid.org/0000-0002-5100-113X

Thomas Bergfeldt − *Institute for Applied Materials (IAM), Karlsruhe Institute of Technology (KIT), 76344 Eggenstein-Leopoldshafen, Germany*

Chittaranjan Das − *Institute for Applied Materials (IAM), Karlsruhe Institute of Technology (KIT), 76344 Eggenstein-Leopoldshafen, Germany*

Michael Heere − *Institute for Applied Materials (IAM), Karlsruhe Institute of Technology (KIT), 76344 Eggenstein-Leopoldshafen, Germany; Heinz Maier-Leibnitz Zentrum (MLZ), Technische Universität München, 85748 Garching, Germany;* orcid.org/0000-0002-7826-1425

Liuda Mereacre − *Institute for Applied Materials (IAM), Karlsruhe Institute of Technology (KIT), 76344 Eggenstein-Leopoldshafen, Germany*

Udo Geckle − *Institute for Applied Materials (IAM), Karlsruhe Institute of Technology (KIT), 76344 Eggenstein-Leopoldshafen, Germany*

Anatoliy Senyshyn − *Heinz Maier-Leibnitz Zentrum (MLZ), Technische Universität München, 85748 Garching, Germany*

Helmut Ehrenberg − *Institute for Applied Materials (IAM), Karlsruhe Institute of Technology (KIT), 76344 Eggenstein-Leopoldshafen, Germany; Helmholtz Institute Ulm (HIU) Electrochemical Energy Storage, 89081 Ulm, Germany;* orcid.org/0000-0002-5134-7130

Michael Knapp − *Institute for Applied Materials (IAM), Karlsruhe Institute of Technology (KIT), 76344 Eggenstein-Leopoldshafen, Germany*

Complete contact information is available at: https://pubs.acs.org/10.1021/acsaem.1c01946

Notes

The authors declare no competing financial interest.

■ ACKNOWLEDGMENTS

This work contributes to the research performed at Center for Electrochemical Energy Storage Ulm-Karlsruhe (CELEST). The authors thank Margarete Offermann for performing BET surface area measurements of all samples. M.H. acknowledges the funding from the project 05K19VK3 "Energy research with Neutrons (ErwiN)" by the German Federal Ministry of Education and Research (BMBF).

■ REFERENCES

(1) Segalini, J.; Daffos, B.; Taberna, P. L.; Gogotsi, Y.; Simon, P. Qualitative Electrochemical Impedance Spectroscopy Study of Ion Transport into Sub-Nanometer Carbon Pores in Electrochemical Double Layer Capacitor Electrodes. *Electrochim. Acta* **2010**, *55*, 7489−7494.

(2) Drabik, E.; Rizos, V. *Prospects for Electric Vehicle Batteries in a Circular Economy: CEPS Research Report*; Centre for European Policy Studies, 2018.

(3) Harper, G.; Sommerville, R.; Kendrick, E.; Driscoll, L.; Slater, P.; Stolkin, R.; Walton, A.; Christensen, P.; Heidrich, O.; Lambert, S.; Abbot, A.; Ryder, K.; Gaines, L.; Anderson, P. Recycling Lithium-Ion Batteries from Electric Vehicles. *Nature* **2019**, *575*, 75−86.

(4) Olsson, L.; Fallahi, S.; Schnurr, M.; Diener, D.; van Loon, P. Circular Business Models for Extended EV Battery Life. *Batteries* **2018**, *4*, No. 57.

(5) Schindler, S.; Bauer, M.; Petzl, M.; Danzer, M. A. Voltage Relaxation and Impedance Spectroscopy as In-Operando Methods for the Detection of Lithium Plating on Graphitic Anodes in Commercial Lithium-Ion Cells. *J. Power Sources* **2016**, *304*, 170−180.

(6) Faenza, N. V.; Lebens-higgins, Z. W.; Mukherjee, P.; Sallis, S.; Pereira, N.; Badway, F.; Halajko, A.; Ceder, G.; Cosandey, F.; Piper, L. F. J.; Amatucci, G. G. Electrolyte-Induced Surface Transformation and Transition Metal Dissolution of Fully Delithiated LiNi0.8-Co0.15Al0.05O2. *Langmuir* **2017**, *33*, 9333−9353.

(7) Zhu, J.; Darma, M. S. D.; Knapp, M.; Sørensen, D. R.; Heere, M.; Fang, Q.; Wang, X.; Dai, H.; Mereacre, L.; Senyshyn, A.; Wei, X.; Ehrenberg, H. Investigation of Lithium-Ion Battery Degradation Mechanisms by Combining Differential Voltage Analysis and Alternating Current Impedance. *J. Power Sources* **2020**, *448*, No. 227575.

(8) Keil, P.; Schuster, S. F.; Travi, J.; Hauser, A.; Karl, R. C.; Jossen, A. Calendar Aging of Lithium-Ion Batteries I. Impact of the Graphite Anode on Capacity Fade. *J. Electrochem. Soc.* **2016**, *163*, 1872−1880.

(9) Ando, K.; Matsuda, T.; Imamura, D. Degradation Diagnosis of Lithium-Ion Batteries with a LiNi0.5Co0.2Mn0.3 and LiMn2O4 Blended Cathode Using DV/DQ Curve Analysis. *J. Power Sources* **2018**, *390*, 278−285.

(10) Wang, J.; Purewal, J.; Liu, P.; Hicks-garner, J.; Soukazian, S.; Sherman, E.; Sorenson, A.; Vu, L.; Tataria, H.; Verbrugge, M. W. Degradation of Lithium Ion Batteries Employing Graphite Negatives and Nickel-Cobalt-Manganese Oxide + Spinel Manganese Oxide Positives: Part 1, Aging Mechanisms and Life Estimation. *J. Power Sources* **2014**, *269*, 937−948.

(11) Kato, H.; Kobayashi, Y.; Miyashiro, H. Differential Voltage Curve Analysis of a Lithium-Ion Battery during Discharge. *J. Power Sources* **2018**, *398*, 49−54.

(12) Sørensen, D. R.; Heere, M.; Zhu, J.; Darma, M. S. D.; Zimnik, S. M.; Mühlbauer, M. J.; Mereacre, L.; Baran, V.; Senyshyn, A.; Knapp, M.; Ehreberg, H. Fatigue in High-Energy Commercial Li Batteries While Cycling at Standard Conditions: An In Situ Neutron Powder Diffraction Study. *ACS Appl. Energy Mater.* **2020**, *3*, 6611−6622.

(13) Sharma, P.; Das, C.; Indris, S.; Bergfeldt, T.; Mereacre, L.; Knapp, M.; Geckle, U.; Ehrenberg, H.; Darma, M. S. D. Synthesis and Characterization of a Multication Doped Mn Spinel, LiNi0.3Cu0.1-Fe0.2Mn1.4O4 as 5 V Positive Electrode Material. *ACS Omega* **2020**, *5*, 22861−22873.

(14) Rodríguez-Carvajal, J. Recent Advances in Magnetic Structure Determination by Neutron Powder Diffraction. *Phys. B* **1993**, *192*, 55−69.

(15) Chan, K. S.; Liang, W.; Chan, C. K. First-Principles Studies of the Lithiation and Delithiation Paths in Si Anodes in Li-Ion Batteries. *J. Phys. Chem. C* **2019**, *123*, 22775−22786.
(16) Yoon, T.; Nguyen, C. C.; Seo, D. M.; Lucht, B. L. Capacity Fading Mechanisms of Silicon Nanoparticle Negative Electrodes for Lithium Ion Batteries. *J. Electrochem. Soc.* **2015**, *162*, A2325−A2330.
(17) Azcarate, I.; Yin, W.; Méthivier, C.; Ribot, F.; Laberty-Robert, C.; Grimaud, A. Assessing the Oxidation Behavior of EC: DMC Based Electrolyte on Non- Catalytically Active Surface. *J. Electrochem. Soc.* **2020**, *167*, No. 080530.
(18) Hwang, S.; Chang, W.; Kim, S. M.; Su, D.; Kim, D. H.; Lee, J. Y.; Chung, K. Y.; Stach, E. A. Investigation of Changes in the Surface Structure of LixNi0.8Co0.15Al0.05O2 Cathode Materials Induced by the Initial Charge. *Chem. Mater.* **2014**, *26*, 1084−1092.
(19) Sallis, S.; Pereira, N.; Mukherjee, P.; Quackenbush, N. F.; Faenza, N.; Schlueter, C.; Lee, T.; Yang, W. L.; Cosandey, F.; Amatucci, G. G.; Piper, L. F. J. Surface Degradation of Li1-xNi0.80Co0.15Al0.05O2 Cathodes: Correlating Charge Transfer Impedance with Surface Phase Transformations. *Appl. Phys. Lett.* **2016**, *108*, No. 263902.
(20) Downie, L. E.; Hyatt, S. R.; Wright, A. T. B.; Dahn, J. R. Determination of the Time Dependent Parasitic Heat Flow in Lithium Ion Cells Using Isothermal Microcalorimetry. *J. Phys. Chem. C* **2014**, *118*, 29533−29541.
(21) Hausbrand, R.; Cherkashinin, G.; Ehrenberg, H.; Gröting, M.; Albe, K.; Hess, C.; Jaegermann, W. Fundamental Degradation Mechanisms of Layered Oxide Li-Ion Battery Cathode Materials: Methodology, Insights and Novel Approaches. *Mater. Sci. Eng., B* **2015**, *192*, 3−25.
(22) Christensen, J.; Newman, J. Stress Generation and Fracture in Lithium Insertion Materials. *J. Solid State Electrochem.* **2006**, *10*, 293−319.
(23) Li, P.; Zhao, Y.; Shen, Y.; Bo, S. Fracture Behavior in Battery Materials. *J. Phys. Energy* **2020**, *2*, No. 022002.
(24) Christensen, J.; Newman, J. A Mathematical Model of Stress Generation and Fracture in Lithium Manganese Oxide. *J. Electrochem. Soc.* **2006**, *153*, A1019.
(25) Zhao, K.; Pharr, M.; Cai, S.; Vlassak, J. J.; Suo, Z. Large Plastic Deformation in High-Capacity Lithium-Ion Batteries Caused by Charge and Discharge. *J. Am. Ceram. Soc.* **2011**, *94*, S226−S235.
(26) Watanabe, S.; Hosokawa, T.; Morigaki, K.; Kinoshita, M.; Nakura, K. Prevention of the Micro Cracks Generation in LiNiCoAlO2 Cathode by the Restriction of DOD. *ECS Trans.* **2012**, *41*, 65−74.
(27) Abraham, D. P.; Spila, T.; Furczon, M. M.; Sammann, E. Evidence of Transition-Metal Accumulation on Aged Graphite Anodes by SIMS. *Electrochem. Solid-State Lett.* **2008**, *11*, A226−A229.
(28) Gallus, D. R.; Schmitz, R.; Wagner, R.; Hoffmann, B.; Nowak, S.; Cekic-laskovic, I.; Schmitz, R. W.; Winter, M. The Influence of Different Conducting Salts on the Metal Dissolution and Capacity Fading of NCM Cathode Material. *Electrochim. Acta* **2014**, *134*, 393−398.
(29) Wandt, J.; Freiberg, A.; Thomas, R.; Gorlin, Y.; Siebel, A.; Jung, R.; Gesteiger, H. A.; Tromp, M. Transition Metal Dissolution and Deposition in Li-Ion Batteries Investigated by Operando X-Ray Absorption Spectroscopy. *J. Mater. Chem. A* **2016**, *4*, 18300−18305.
(30) Darma, M.; Lang, M.; Kleiner, K.; Mereacre, L.; Liebau, V.; Fauth, F.; Bergfeldt, T.; Ehrenberg, H. The Influence of Cycling Temperature and Cycling Rate on the Phase Specific Degradation of a Positive Electrode in Lithium Ion Batteries: A Post Mortem Analysis. *J. Power Sources* **2016**, *327*, 714−725.
(31) Tsubouchi, S.; Domi, Y.; Doi, T.; Ochida, M.; Nakagawa, H.; Yamanaka, T.; Abe, T.; Ogumi, Z. Spectroscopic Characterization of Surface Films Formed on Edge Plane Graphite in Ethylene Carbonate-Based Electrolytes Containing Film- Forming Additives. *J. Electrochem. Soc.* **2012**, *159*, A1786.
(32) Zhang, J.; Wang, R.; Yang, X.; Lu, W.; Wu, X.; Wang, X.; Li, H.; Chen, L. Direct Observation of Inhomogeneous Solid Electrolyte Interphase on MnO Anode with Atomic Force Microscopy and Spectroscopy. *Nano Lett.* **2012**, *12*, 2153−2157.
(33) Shin, H.; Park, J.; Han, S.; Marie, A.; Lu, W. Component- / Structure-Dependent Elasticity of Solid Electrolyte Interphase Layer in Li-Ion Batteries: Experimental and Computational Studies. *J. Power Sources* **2015**, *277*, 169−179.
(34) Chan, C. K.; Ruffo, R.; Hong, S. S.; Cui, Y. Surface Chemistry and Morphology of the Solid Electrolyte Interphase on Silicon Nanowire Lithium-Ion Battery Anodes. *J. Power Sources* **2009**, *189*, 1132−1140.
(35) Veith, G. M.; Doucet, M.; Baldwin, J. K.; Sacci, R. L.; Fears, T. M.; Wang, Y.; Browning, J. F. Composition as a Function of State of Charge on a Silicon Anode. *J. Phys. Chem. C* **2015**, *119*, 20339−20349.
(36) Lebens-higgins, Z. W.; Sallis, S.; Faenza, N. V.; Badway, F.; Pereira, N.; Halat, D. M.; Wahila, M.; Schlueter, C.; Lee, T.; Yang, W.; Grey, C. P.; Amatucci, G. G.; Piper, L. F. J. Evolution of the Electrode-Electrolyte Interface of LiNi0.8Co0.15Al0.05O2 Electrodes Due to Electrochemical and Thermal Stress. *Chem. Mater.* **2018**, *30*, 958−969.
(37) Jung, R.; Metzger, M.; Haering, D.; Solchenbach, S.; Marino, C.; Tsiouvaras, N.; Stinner, C.; Gasteiger, H. A. Consumption of Fluoroethylene Carbonate (FEC) on Si-C Composite Electrodes for Li-Ion Batteries. *J. Electrochem. Soc.* **2016**, *163*, A1705−A1716.
(38) Wetjen, M.; Pritzl, D.; Jung, R.; Solchenbach, S.; Ghadimi, R.; Gasteiger, H. A. Differentiating the Degradation Phenomena in Silicon-Graphite Electrodes for Lithium-Ion Batteries. *J. Electrochem. Soc.* **2017**, *164*, A2840−A2852.
(39) Xu, C.; Lindgren, F.; Philippe, B.; Gorgoi, M.; Björefors, F.; Edström, K.; Gustafsson, T. Improved Performance of the Silicon Anode for Li-Ion Batteries: Understanding the Surface Modification Mechanism of Fluoroethylene Carbonate as an Effective Electrolyte Additive. *Chem. Mater.* **2015**, *27*, 2591−2599.
(40) Laresgoiti, I.; Käbitz, S.; Ecker, M.; Uwe, D. U. Modeling Mechanical Degradation in Lithium Ion Batteries during Cycling: Solid Electrolyte Interphase Fracture. *J. Power Sources* **2015**, *300*, 112−122.
(41) Qi, Y.; Guo, H.; Hector, L. G.; Timmons, A. Threefold Increase in the Young's Modulus of Graphite Negative Electrode during Lithium Intercalation. *J. Electrochem. Soc.* **2010**, *157*, A558−A566.
(42) Cannarella, J.; Arnold, C. B. The Effects of Defects on Localized Plating in Lithium-Ion Batteries. *J. Electrochem. Soc.* **2015**, *162*, A1365−A1373.
(43) Fuchs, G.; Willenberg, L.; Ringbeck, F.; Sauer, D. U. Post-mortem Analysis of Inhomogeneous Induced Pressure on Commercial Lithium-Ion Pouch Cells and Their Effects. *Sustainability* **2019**, *11*, No. 6738.
(44) Günter, F. J.; Habedank, J. B.; Schreiner, D.; Neuwirth, T.; Gilles, R.; Reinhart, G. Introduction to Electrochemical Impedance Spectroscopy as a Measurement Method for the Wetting Degree of Lithium-Ion Cells Introduction to Electrochemical Impedance Spectroscopy as a Measurement Method for the Wetting Degree of Lithium-Ion Cells. *J. Electrochem. Soc.* **2018**, *165*, A3249−A3256.
(45) Ogihara, N.; Itou, Y.; Kawauchi, S. Ion Transport in Porous Electrodes Obtained by Impedance Using a Symmetric Cell with Predictable Low-Temperature Battery Performance. *J. Phys. Chem. Lett.* **2019**, *10*, 5013−5018.
(46) Stiaszny, B.; Ziegler, J. C.; Krauß, E. E.; Zhang, M.; Schmidt, J. P.; Ivers-tiffee, E. Electrochemical Characterization and Post -Martern Analysis of Aged LiMn204 -NMC / Graphite Iithium Ion Batteries Part II: Calendar Aging. *J. Power Sources* **2014**, *258*, 61−75.
(47) An, S. J.; Li, J.; Mohanty, D.; Daniel, C.; Polzin, B. J.; Croy, J. R.; Trask, S.; Wood, D. L. Correlation of Electrolyte Volume and Electrochemical Performance in Lithium-Ion Pouch Cells with Graphite Anodes and NMC532 Cathodes. *J. Electrochem. Soc.* **2017**, *164*, A1195−A1202.
(48) Günter, F. J.; Burgstaller, C.; Konwitschny, F.; Reinhart, G. Influence of the Electrolyte Quantity on Lithium-Ion Cells. *J. Electrochem. Soc.* **2019**, *166*, A1709−A1714.

https://doi.org/10.1021/acsaem.1c01946
ACS Appl. Energy Mater. 2021, 4, 9982−10002

(49) Zhou, X.; Pan, Z.; Han, X.; Lu, L.; Ouyang, M. An Easy-to-Implement Multi-Point Impedance Technique for Monitoring Aging of Lithium Ion Batteries. *J. Power Sources* **2019**, *417*, 188−192.
(50) Love, C. T.; Swider-Lyons, K. Impedance Diagnostic for Overcharged Lithium-Ion Batteries. *Electrochem. Solid-State Lett.* **2012**, *15*, A53.
(51) Love, C. T.; Virji, M. B. V.; Rocheleau, R. E.; Swider-lyons, K. E. State-of-Health Monitoring of 18650 4S Packs with a Single-Point Impedance Diagnostic. *J. Power Sources* **2014**, *266*, 512−519.
(52) Kleiner, K.; Ehrenberg, H. Challenges Considering the Degradation of Cell Components in Commercial Lithium-Ion Cells: A Review and Evaluation of Present Systems. *Top. Curr. Chem.* **2017**, No. 54.
(53) Schmidt, H.; Jerliu, B.; Hüger, E.; Stahn, J. Volume Expansion of Amorphous Silicon Electrodes during Potentiostatic Lithiation of Li-Ion Batteries. *Electrochem. Commun.* **2020**, *115*, No. 106738.
(54) Hahn, M.; Buqa, H.; Ruch, P. W.; Goers, D.; Spahr, M. E.; Ufheil, J.; Novak, P.; Kötz, R. A Dilatometric Study of Lithium Intercalation into Powder-Type Graphite Electrodes. *Electrochem. Solid-State Lett.* **2008**, *11*, A151−A154.
(55) Lang, M.; Darma, M. S. D.; Kleiner, K.; Riekehr, L.; Mereacre, L.; Pérez, M. A.; Ehrenberg, H.; Liebau, V. Post Mortem Analysis of Fatigue Mechanisms in LiNi0.8Co0.15 Al0.02O2-LiNi0.5Co0.2Mn0.3O2-LiMn2O4/Graphite Lithium Ion Batteries. *J. Power Sources* **2016**, *326*, 397−409.
(56) Stiaszny, B.; Ziegler, J. C.; Krauß, E. E.; Schmidt, J. P.; Iverstiffée, E. Electrochemical Characterization and Post-Mortem Analysis of Aged LiMn2O4-Li(Ni052Mn0.3Co0.2)/Graphite Lithium Ion Batteries. Part I: Cycle Aging. *J. Power Sources* **2014**, *251*, 439−450.
(57) Wang, J.; Purewal, J.; Liu, P.; Hicks-garner, J.; Soukazian, S.; Sherman, E.; Sorenson, A.; Vu, L.; Tataria, H.; Verbrugge, M. W. Degradation of Lithium Ion Batteries Employing Graphite Negatives and Nickel-Cobalt-Manganese Oxide + Spinel Manganese Oxide Positives: Part 1, Aging Mechanisms and Life Estimation. *J. Power Sources* **2014**, *269*, 937−948.
(58) Zheng, Y.; He, Y.; Qian, K.; Li, B.; Wang, X.; Li, J.; Chiang, S. W.; Miao, C.; Kang, F.; Zhang, J. Deterioration of Lithium Iron Phosphate/Graphite Power Batteries under High-Rate Discharge Cycling. *Electrochim. Acta* **2015**, *176*, 270−279.
(59) Yao, K. P. C.; Okasinski, J. S.; Kalaga, K.; Shkrob, I. A.; Abraham, D. P. Quantifying Lithium Concentration Gradients in the Graphite Electrode of Li-Ion Cells Using Operando Energy Dispersive X-Ray Diffraction. *Energy Environ. Sci.* **2019**, *12*, 656−665.
(60) Senyshyn, A.; Mühlbauer, M. J.; Nikolowski, K.; Pirling, T.; Ehrenberg, H. " In-Operando" Neutron Scattering Studies on Li-Ion Batteries. *J. Power Sources* **2012**, *203*, 126−129.
(61) Letellier, M.; Chevallier, F.; Beguin, F. In Situ 7 Li NMR during Lithium Electrochemical Insertion into Graphite and a Carbon/Carbon Composite. *J. Phys. Chem. Solids* **2006**, *67*, 1228−1232.
(62) Börner, M.; Friesen, A.; Grützke, M.; Stenzel, Y. P.; Brunklaus, G.; Haetge, J.; Nowak, S.; Schappacher, F. M.; WInter, M. Correlation of Aging and Thermal Stability of Commercial 18650-Type Lithium Ion Batteries. *J. Power Sources* **2017**, *342*, 382−392.
(63) Hua, W.; Schwarz, B.; Azmi, R.; Müller, M.; Darma, M. S. D.; Knapp, M.; Senyshyn, A.; Heere, M.; Missyul, A.; Simonelli, L.; Binder, J. R.; Indris, S.; Ehrenberg, H. Lithium-Ion (de)Intercalation Mechanism in Core-Shell Layered Li(Ni,Co,Mn)O2 Cathode Materials. *Nano Energy* **2020**, *78*, No. 105231.
(64) Park, J.; Soc, J. E.; Park, J.; Lu, W.; Marie, A. Numerical Simulation of Stress Evolution in Lithium Manganese Dioxide Particles Due to Coupled Phase Transition and Intercalation Numerical Simulation of Stress Evolution in Lithium Manganese Dioxide Particles Due to Coupled Phase Transition and Intercala. *J. Electrochem. Soc.* **2011**, *158*, A201.
(65) Heere, M.; Mühlbauer, M. J.; Schökel, A.; Knapp, M.; Ehrenberg, H.; Senyshyn, A. Energy Research with Neutrons (ErwiN) and Installation of a Fast Neutron Powder Diffraction Option at the MLZ, Germany. *J. Appl. Crystallogr.* **2018**, *51*, 591−595.

https://doi.org/10.1021/acsaem.1c01946
ACS Appl. Energy Mater. 2021, 4, 9982−10002